

ABSCHLUSSARBEIT IM MASTERSTUDIENGANG  
PHYSIK DER KONDENSIERTEN MATERIE

**Direct Generation of an Ultra  
Broadband Spectrum from  
Ytterbium Doped Thin-Disk Lasers**

**Autor:**

Theresa Buberl

**Betreuer:**

Dr. Hanieh Fattahi

Prof. Dr. Reinhard Kienberger

Prof. Dr. Ferenc Krausz

31. März 2016







## Zusammenfassung

Dioden gepumpte, Ytterbium dotierte Scheibenlaser mit einer Pulsdauer von 1 ps werden den Stand der Technik für optisch parametrische Verstärkung mit gestreckten Pulsen (OPCPA) revolutionieren. Mit ihrer skalierbaren Energie und Leistung, sowie ihrer Emissionswellenlänge von  $1 \mu\text{m}$  bieten sie bedeutende Vorteile gegenüber den bisher verwendeten Ti:Sa Lasern. Die Kombination mehrerer OPCPA-Kanäle mit unterschiedlichen Wellenlängenbereichen wird die Entwicklung eines E-Feld-Synthesizers ermöglichen, der in der Lage ist, Lichtwellenformen mit unerreichter Energie und Leistung zu erzeugen. Da diese Lichtwellenformen weniger als eine Schwingungsdauer des elektrischen Feldes umfassen, sind sie im Hinblick auf das Verschieben der Maximalenergie für die Generierung von hohen Harmonischen (HHG) in den Bereich harter Röntgenstrahlen vielversprechend.

Eine der Hauptanforderungen für die Entwicklung eines solchen Synthesizers ist die Verfügbarkeit eines ultrabreitbandigen, stabilen Kontinuums mit einer stetigen spektralen Phase, das als Signal für die verschiedenen OPCPA-Kanäle dient. Im Allgemeinen ist die bevorzugte Methode um breitbandige Signale für OPCPA zu erzeugen Superkontinuum-Generierung in optischen Fasern oder in kompakten, nichtlinearen Medien. Wenn die Pulsdauer der Eingangssignale im ps-Bereich liegt, weisen die erzeugten Spektren allerdings Energieschwankungen und mangelnde Kohärenz auf. Um diese Nachteile zu umgehen sind Methoden zur Pulskomprimierung von Pulsen mit Picosekundendauer zu Pulsen mit einer Dauer von wenigen hundert Femtosekunden erforderlich, die stabile Filamente in optischen Fasern und kompakten, nichtlinearen Medien erlauben. Dazu werden in dieser Arbeit zwei verschiedene Ansätze vorgestellt und miteinander verglichen.

Der erste Ansatz basiert auf Cross-polarized Wave Generation (XPW), einem nichtlinearen Effekt dritter Ordnung, und ermöglicht eine Kompressionsrate von mehr als drei in einem kaskadierten Aufbau. Dabei werden die Eingangspulse mit einer Dauer von 1 ps zu Pulsen komprimiert, die kürzer als 250 fs sind. Die Konversionseffizienz des vorgeschlagenen Systems ist niedrig, aber die Ausgangspulse sind intrinsisch komprimiert und haben ein verbessertes Strahlprofil, sowie ein glatteres Spektrum. Der zweite Ansatz basiert auf kaskadierten Nichtlinearitäten zweiter Ordnung und ermöglicht daher höhere Konversionseffizienzen. Bei der phasenunangepassten Erzeugung der zweiten Harmonischen (SHG) wird die Fundamentale spektral verbreitert und kann anschließend durch dispersive Elemente zeitlich komprimiert werden. Der verwendete Aufbau ist in der Lage, die Eingangspulse mit einer Dauer von 1 ps zu Pulsen mit einer Dauer von 150 fs bei einer Konversionseffizienz von 45 % zu verkürzen. Die Kompressionsrate von mehr als sechs wird durch einen zweistufigen Aufbau erreicht. Durch eine Optimierung des Systems könnte seine Konversionseffizienz auf 60 % erhöht werden. Die skalierbare Eingangsenergie, der hohe zeitliche Kontrast und die Einfachheit beider Techniken machen sie zu attraktiven Methoden für die Erzeugung von OPCPA-Signal aus Yb:YAG Scheibenlasern.

Die erzeugten energetischen 150 fs Pulse wurden verwendet, um ein neuartiges Konzept zu testen, das die Kontinuums-Generierung mit mehreren dünnen Plättchen ermöglicht. Dieser kompakte, robuste Aufbau ist einfach zu bedienen und vielversprechend, was die Eingangsenergie und die Konversionseffizienz im Vergleich zu optischen Fasern betrifft. In Vorversuchen gelang die Komprimierung von 150 fs Pulsen zu 60 fs Pulsen mit drei dünnen Glasplättchen. Diese Ergebnisse können ansatzweise das Potential der Methode demonstrieren und zu weiterer experimenteller sowie numerischer Analyse anregen.

## Abstract

Diode-pumped Ytterbium-doped thin-disk lasers with 1-ps pulse duration are going to revolutionize the current state of the art of optical parametric chirped pulse amplifiers (OPCPA). With their scalability in power and energy and their emission wavelength near  $1\ \mu\text{m}$  they offer substantial advantages towards the commonly used Ti:Sa lasers. By combining several OPCPA channels at different spectral ranges these technological advances will allow us to develop a field synthesizer capable of generating sub-cycle waveforms at unseen peak and average power. Such a device holds promise to push the energy cut-off of high harmonic generation to the hard x-ray regime.

A major requirement for developing such a field synthesizer is an ultra broadband, stable supercontinuum with a well-behaved spectral phase to seed the different OPCPA channels. Supercontinuum generation in bulk and fibers driven by hundreds-fs pulses is the current method of choice for generating the OPCPA seed pulses. However, when the process is triggered by longer pulses in the order of ps, the generated spectrum shows imperfect coherence and energy fluctuations. Avoiding these drawbacks demands for pulse shortening of 1-ps pulses down to several hundreds of fs, where stable filamentation in fiber or bulk can be achieved.

By presenting and comparing two different methods for the compression of 1 ps pulses, this thesis shows alternative concepts which prevent the mentioned problems. The first method is based on the third-order nonlinear process of cross-polarized wave generation (XPW). In a cascaded XPW setup we realized the compression of 1 ps pulses by more than a factor of four to below 250 fs. The conversion efficiency of the system is below 1 %, but it offers the advantages of beam profile enhancement, spectral smoothing, and intrinsic pulse shortening.

The second method is based on cascaded second-order nonlinearities and therefore helps to increase the conversion efficiency. In phase mismatched second harmonic generation (SHG) the fundamental is spectrally broadened and can then be compressed in time by dispersive elements. The employed setup is capable of compressing 1 ps pulses to 150 fs at a conversion efficiency of 45 %. The compression rate of above six is achieved in a two-stage approach. Optimizing the system will allow to raise the conversion efficiency up to 60 %. The energy scalability, the good temporal contrast and the simplicity of both techniques make them a desirable approach for generating OPCPA seed pulses from Yb:YAG thin-disk lasers.

Having energetic 150 fs pulses in place, we tested a novel continuum generation approach conducted in multiple thin plates. This approach is compact, robust and simple to operate and holds promise to outperform spectral broadening in fibers in terms of input energy and conversion efficiency. In our preliminary experiments we could further compress the 150 fs pulses to below 60 fs using three thin fused silica plates. These results show the potential of this method to some extent and motivate further experimental and numerical study.



# Contents

|          |  |           |
|----------|--|-----------|
| <b>1</b> | <b>Towards hard x-ray attosecond pulses</b>                          | <b>1</b>  |
| <b>2</b> | <b>How to shorten 1 ps pulses</b>                                    | <b>5</b>  |
| 2.1      | Large mode area fibers . . . . .                                     | 5         |
| 2.2      | Hollow core fibers . . . . .   | 6         |
| 2.3      | Spectral broadening in bulk . . . . .                                | 7         |
| 2.4      | Summary and conclusion . . . . .                                     | 8         |
| <b>3</b> | <b>Cross Polarized Wave Generation</b>                               | <b>10</b> |
| 3.1      | Basic understanding of the process . . . . .                         | 10        |
| 3.2      | Experimental setup for cascaded XPW . . . . .                        | 15        |
| 3.3      | Experimental results . . . . .                                       | 18        |
| 3.3.1    | Influence of different third-order nonlinearities . . . . .          | 19        |
| 3.3.2    | Influence of the spectral phase . . . . .                            | 23        |
| 3.4      | Summary and conclusion . . . . .                                     | 27        |
| <b>4</b> | <b>Cascaded second-order nonlinearities</b>                          | <b>29</b> |
| 4.1      | Phase modulation in second-order nonlinear processes . . . . .       | 29        |
| 4.2      | Experimental setup for pulse compression with cascaded SHG . . . . . | 34        |
| 4.3      | Experimental results . . . . .                                       | 36        |
| 4.3.1    | Influence of the input intensity . . . . .                           | 38        |
| 4.3.2    | Spatial characterization of the spectrum . . . . .                   | 40        |
| 4.4      | Summary and conclusion . . . . .                                     | 41        |
| <b>5</b> | <b>Spectral broadening using multiple thin plates</b>                | <b>42</b> |
| 5.1      | Self-phase modulation and self-focusing in thin plates . . . . .     | 42        |
| 5.2      | Experimental setup . . . . .   | 43        |
| 5.3      | Experimental results . . . . .                                       | 45        |
| 5.3.1    | Spectral broadening with 0.3 mm fused silica plates . . . . .        | 45        |
| 5.3.2    | Pulse compression . . . . .  | 47        |
| 5.3.3    | Spatial characterization of the spectrum . . . . .                   | 47        |
| 5.3.4    | Further broadening after compression . . . . .                       | 49        |
| 5.4      | Summary and conclusion . . . . .                                     | 50        |
| <b>6</b> | <b>Conclusion and outlook</b>  | <b>52</b> |

|                   |   |           |
|-------------------|---|-----------|
| <b>Appendix A</b> | <b>Frequency-resolved optical gating: Measuring ultrashort pulses</b> | <b>55</b> |
| A.1               | The phase-dilemma . . . . .   | 55        |
| A.2               | Beam geometry of a second-harmonic-generation FROG . . . . .          | 55        |
| A.3               | Retrieving the electric field from the spectrogramm . . . . .         | 56        |
| <b>Appendix B</b> | <b>Simulation of the XPW process</b>                                  | <b>58</b> |

# List of Figures

|      |   |    |
|------|---|----|
| 1.1  | Schematic architecture of the field synthesizer . . . . .   | 3  |
| 2.1  | Different types of photonic crystal fiber . . . . .   | 6  |
| 3.1  | Scheme of the XPW process . . . . .   | 11 |
| 3.2  | XPW conversion efficiency as a function of the phasematching angle . . . . .                                    | 12 |
| 3.3  | XPW conversion efficiency as a function of peak intensity on the crystal . . . . .                              | 14 |
| 3.4  | Dependence of the XPW conversion efficiency on the beam divergence . . . . .                                    | 15 |
| 3.5  | Sketch of the setup for cascaded XPW . . . . .  | 16 |
| 3.6  | Calculated GDD of a pair of transmission gratings . . . . .   | 17 |
| 3.7  | Characterization of the input pulse and the XPW pulse after each stage . . . . .                                | 18 |
| 3.8  | Influence of conversion efficiency on spectral width and pulse duration . . . . .                               | 20 |
| 3.9  | Influence of different third-order effects . . . . .  | 21 |
| 3.10 | Simulated XPW spectra for different nonlinearities . . . . .  | 22 |
| 3.11 | GDD of the XPW pulse . . . . .  | 23 |
| 3.12 | Comparison between the XPW pulse for compressed and uncompressed input pulse . . . . .                          | 24 |
| 3.13 | Simulated broadening factor for input pulses with increasing GDD . . . . .                                      | 25 |
| 3.14 | Pulse compression . . . . .   | 26 |
| 3.15 | Influence of the spectral phase on XPW . . . . .  | 27 |
| 4.1  | Depletion and nonlinear phase shift of the fundamental in cascaded SHG . . . . .                                | 30 |
| 4.2  | Spectra and beam profiles of the fundamental wave for different phase mismatch . . . . .                        | 32 |
| 4.3  | Spectral broadening and conversion efficiency of the fundamental in BBO and LBO . . . . .                       | 33 |
| 4.4  | Sketch of the cascaded SHG setup . . . . .  | 34 |
| 4.5  | Transmission of the different optical components . . . . .  | 35 |
| 4.6  | Characterization of the input pulse and the compressed pulses after each phase mismatched SHG crystal . . . . . | 37 |
| 4.7  | Spectra after SHG in LBO and in BBO consecutively for different input energies . . . . .                        | 38 |
| 4.8  | Pulse duration and beam profile of the pulse after each grating compressor . . . . .                            | 39 |
| 4.9  | Spectra of the fundamental for different centrosymmetric fractions of the beam . . . . .                        | 40 |
| 5.1  | Sketch of the multiple thin plates broadening approach . . . . .  | 44 |
| 5.2  | Spectra and transmission for different combinations of thin plates . . . . .                                    | 46 |

|     |   |    |
|-----|---|----|
| 5.3 | Spectrogram and retrieved time envelope and spectrum of the pulse after compression . . . . . | 48 |
| 5.4 | Spatial characterization of the broadened spectrum . . . . .                                  | 49 |
| 5.5 | Comparison between the spectra before and after compression . . . . .                         | 50 |
| A.1 | Schematic beam geometry for a SHG-FROG . . . . .  | 56 |

## List of Tables

|     |  |    |
|-----|--|----|
| 3.1 | Parameters of the input pulse and the XPW pulse after each stage . . . . . | 19 |
|-----|--|----|

## **Acronyms**

|              |  |
|--------------|--|
| <b>BBO</b>   | Bariumborate                                   |
| <b>CEP</b>   | Carrier envelope phase                         |
| <b>DFG</b>   | Difference frequency mixing                    |
| <b>FROG</b>  | Frequency resolved optical gating              |
| <b>FT</b>    | Fourier transform                              |
| <b>FWHM</b>  | Full width at half maximum                     |
| <b>GDD</b>   | Group delay dispersion                         |
| <b>HCF</b>   | Hollow core fiber                              |
| <b>HHG</b>   | High harmonic generation                       |
| <b>LBO</b>   | Lithiumtriborate                               |
| <b>LMA</b>   | Large mode area fiber                          |
| <b>MIR</b>   | Mid infrared                                   |
| <b>NIR</b>   | Near infrared                                  |
| <b>OPA</b>   | Optical parametric amplification               |
| <b>OPCPA</b> | Optical parametric chirped pulse amplification |
| <b>PCF</b>   | Photonic crystal fiber                         |
| <b>SHG</b>   | Second harmonic generation                     |
| <b>SPM</b>   | Self-phase modulation                          |
| <b>TFP</b>   | Thin film polarizer                            |
| <b>UV</b>    | Ultra violet                                   |
| <b>VIS</b>   | visible  |
| <b>XUV</b>   | Extreme ultra violet                           |
| <b>XPM</b>   | Cross-phase modulation                         |
| <b>XPW</b>   | Cross-polarized wave generation                |
| <b>YAG</b>   | Yttrium aluminum garnet                        |



# Chapter 1

## Towards hard x-ray attosecond pulses

Attosecond ( $10^{-18}$  s) science is thought to be one of the most dynamically expanding research fields of the new millennium. By providing techniques to produce and measure signals with the duration of quadrillionths of a second, attosecond science gives insight into electron dynamics on their real time scale. The understanding of electron processes in atoms, molecules, and solids is substantial for physics, life science, medicine and technology.

The first step towards attosecond science was made in 1960 with the realization of the laser (Light Amplification by Stimulated Emission of Radiation) [1]. In comparison to common light sources, the electric field of the photons in a laser beam oscillates coherently and provides intensities not achievable before. From the continuous waves emitted by the first lasers to light pulses on the time scale of electron motion, many technological challenges had to be overcome.

Gain-switching opened up the possibility to produce laser pulses from continuous waves [2]. With Kerr lens mode locking the pulse duration could be decreased from a few picoseconds to the femtosecond regime [3]. With the availability of femtosecond pulses, the field of ultrafast science developed. It became possible to follow processes like the formation and breaking of chemical bonds on their real timescale. Using extracavity pulse compression, pulses shorter than 5 fs were produced [4].

Pulses of such short duration comprise only a few oscillation cycles of the electromagnetic field of the light. Their ultimate duration is limited by the laser oscillation period  $T_0 = \lambda_L/c$ , where  $c$  is the speed of light and  $\lambda_L$  the laser carrier wavelength [5]. To break the femtosecond-barrier, the carrier wavelength needs to be shifted to the XUV or x-ray regime. Therefore gases are irradiated with intense, few-cycle femtosecond pulses to produce high harmonics of the VIS or NIR [6]. Upon the recombination of electrons with their parent gas ions after one half-cycle of the driving electric field, the emission of 250 as pulse trains was observed [7]. With the generation and measurement of the first single, isolated soft x-ray attosecond pulse all requirements for time resolved spectroscopy on the sub-femtosecond scale were met [8].

Signals with the duration of attoseconds allow us to temporally resolve faster and faster processes. For example, electron dynamics in semiconductor nanostructures, molecular orbitals, and inner atomic shells happen on the timescale of attoseconds [9]. With pump-probe spectroscopy it became possible to follow the motion of individual electrons in inner atomic shells [10]. By observing the high harmonic generation (HHG) spectrum of molecules, con-

clusions on their instantaneous, orbital structures can be drawn [11, 12].

To reach the ultimate frontiers of physics we need to push the energy cut-off of HHG towards the hard x-ray regime. In this way attosecond pulses with Ångström-wavelength can be generated to allow for spatial resolution on the atomic scale [13]. At the same time, shorter wavelength translates into higher energy, which enables excitation processes not accessible with the current attosecond sources.

By mixing few cycle NIR pulses with their second harmonic to produce a 1.5 cycle driver waveform, Cavalieri et al. [14] were able to increase the flux and photon energy of HHG. Moulet et al. [15] showed that multi-octave, sub-cycle light transients available from field synthesizers offer the potential to extend the HHG photon energy to the hard x-ray regime.

Such field synthesizers permit the attosecond precise tailoring of the electric field of waveforms confinable to less than a single cycle of its carrier wave [16]. Hereto an ultrabroadband continuum is spectrally divided into its constituent wavepackets, the properties of the wavepackets are modified, and in the last step all components of the continuum are superimposed to synthesize a light transient [17].

The multi-terawatt waveform synthesizer currently under development in the Laboratory of Extreme Photonics (LEX) in Garching combines the capacity of light transient tailoring with the benefits of Ytterbium-doped thin-disk laser technology. This technology provides robust performance, scalability in power and energy, and a longer central emission wavelength than Ti:Sa lasers [18]. Since the energy cut-off of HHG scales with the wavelength of the driving pulse [19], Yb-doped lasers are preferred to the commonly used Ti:Sa lasers.

At the same time, the 1 ps pulses yielded from Yb-doped thin-disk regenerative amplifiers [20] are optimal to pump optical parametric chirped-pulse amplification (OPCPA). The pulse duration of 1 ps allows the best trade-off between amplification bandwidth and conversion efficiency [21]. OPCPAs driven by kilowatt scale pulses from Yb-doped lasers at petawatt scale peak power can combine high average and high peak power in ultrashort pulses for the first time [22]. Because of its innovativeness, this approach was termed third-generation femtosecond technology. Bringing together third-generation femtosecond technology and waveform synthesizing to produce high average and high peak power, sub-cycle driving pulses for HHG, holds promise to enable attosecond pulses at unseen photon energies and photon fluxes.

Figure 1.1 shows the schematic architecture of a three-channel OPCPA field synthesizer driven by a Yb:YAG thin-disk regenerative amplifier. The amplifier is seeded by a Yb:YAG thin-disk oscillator and works at a repetition rate of 5 kHz. It delivers 1 ps pulses centered at 1030 nm with a pulse energy of 20 mJ. A fraction of this energy is used to generate the ultra-broadband OPCPA seed spanning from 450 nm to 2.7  $\mu\text{m}$ . Using suitable optics this continuum is separated into three channels centered at 550 nm, 1  $\mu\text{m}$  and 2.1  $\mu\text{m}$ . The different OPCPA channels are pumped by the fundamental, the second harmonic, and their sum-frequency. Each of them supports few-cycle pulses. The output of the channels can be superimposed to synthesize sub-cycle light transients. By changing the energy ratio and the delay between the channels, the shape of their composed electric field can be modified.

To avoid an active pump-seed stabilization system, pump and seed are generated from the output of the regenerative amplifier. An essential criterion to guarantee the controllable

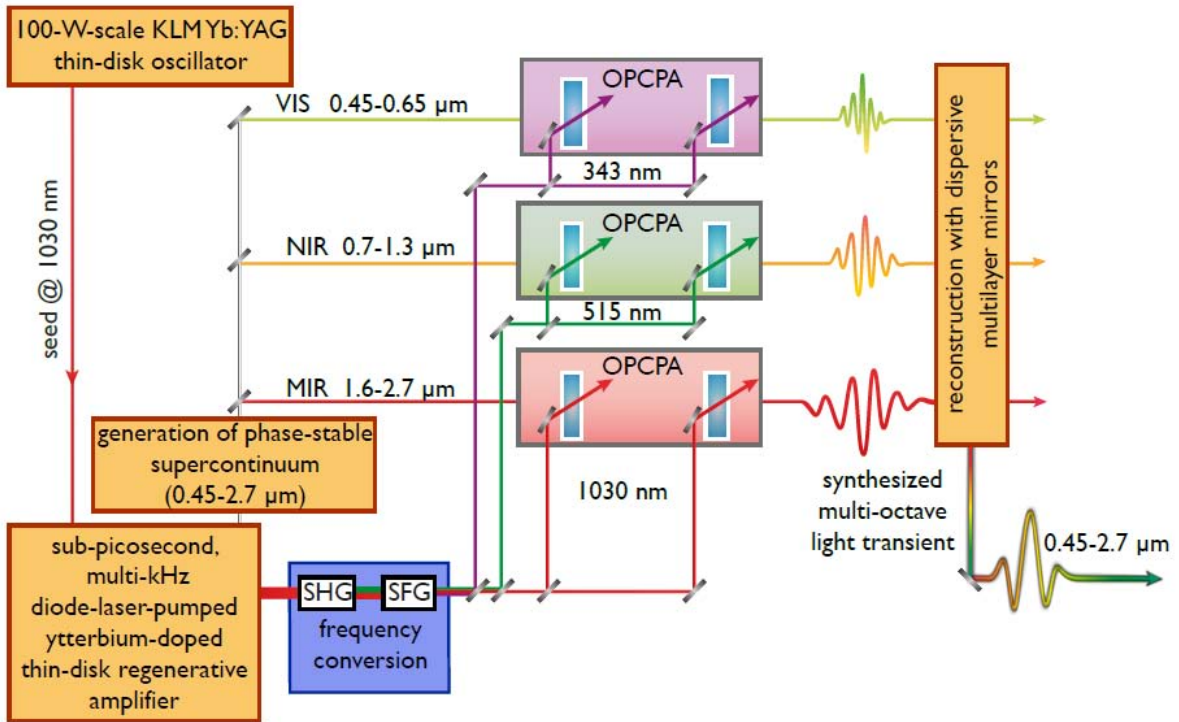


**Figure 1.1:** Schematic architecture of a three-channel OPCPA field synthesizer: The system is driven by 20 mJ, 1 ps pulses centered at 1030 nm from a Yb-YAG thin-disk regenerative amplifier seeded by a Yb-YAG thin-disk oscillator. The ultra broadband seed is separated in three channels centered at the VIS, the NIR and the MIR. The OPCPAs are pumped by the fundamental, the second harmonic and their sum-frequency. All three channels provide few-cycle pulses. By synthesizing them shapeable, sub-cycle light transients can be produced. Adapted from: "Third-generation femtosecond technology", by H. Fattahi, 2014, Dissertation, Ludwig-Maximilians-Universität Munich, p. 137.

manipulation of the waveform is the carrier-envelope-phase (CEP) stability of the seed. This requirement can be fulfilled by difference frequency generation (DFG). DFG is an intrinsically CEP-stable process and shifts the spectrum to longer wavelengths [23]. Generating a broadband DFG signal is only possible in short crystals to avoid temporal separation of the different frequencies due to dispersion [22]. To reach reasonable conversion efficiency in DFG with short crystals the input pulses need to be significantly shorter than the 1 ps pulses from the regenerative amplifier. With a suitable compression stage in hand, the generation of an ultra broadband, phase-stable seed covering more than two octaves of the spectrum would become feasible by combining DFG and spectral broadening in a hollow-core fiber.

The contribution of this thesis on the way towards hard x-ray attosecond pulses is to present a suitable concept for the direct generation of a broadband continuum from 1 ps

pulses. In Chapter 2 common spectral broadening techniques and their suitability for 1 ps pulses are discussed. Because all of these techniques show major drawbacks when operated with 1 ps input pulses, this thesis offers two alternative approaches.

Chapter 3 addresses the first approach which is based on cross-polarized wave generation (XPW). In this third-order nonlinear process pulses with orthogonal polarization with respect to the input pulse are generated. The XPW pulses offer temporal contrast improvement, spectral smoothing, and spatial beam profile enhancement. Besides these positive effects, pulses are spectrally broadened and temporally shortened by  $\sqrt{3}$  during XPW. We take advantage of the intrinsically shorter XPW pulses in a cascaded setup. By repeating the XPW process twice and separating the input pulse after each XPW process, we reach pulse shortening and spectral broadening by more than a factor of 3. Our numerical results explain the experimentally observed additional broadening by an interplay of other third-order nonlinear effects. We could also identify that chirp decreases spectral broadening and pulse shortening during XPW.

Chapter 4 offers an alternative approach based on cascaded second-order nonlinearities. Phase-mismatched second harmonic generation causes a back-conversion from the second harmonic to the fundamental. The phase shift introduced during back-conversion is comparable to the Kerr effect. Due to self-focusing followed by self-phase modulation the fundamental experiences spectral broadening. We designed a setup consisting of two phase mismatched SHG crystals followed by grating compressors. It turned out that this setup is a promising approach to shorten 1 ps input pulses to less than 150 fs. The total conversion efficiency of the system is 45 % and can easily be optimized to more than 60 %.

In Chapter 5 the 150 fs output pulses of this system are used to test a novel spectral broadening technique in fused silica. Lu et al. [24] proposed to use multiple thin plates instead of the common spectral broadening in bulk. This approach holds promise to outperform fiber spectral broadening in terms of input power and conversion efficiency. With three fused silica plates we managed to generate a spectrum ranging from 990 nm to 1060 nm and compress it to less than 60 fs. By focusing the compressed pulses to another plate, we achieved a spectrum which extends from 980 nm to 1065 nm and supports a FT limit pulse duration of 36 fs.

Chapter 6 summarizes the results, compares the different pulse shortening approaches and gives a proposal for a direct broadband seed generation scheme from 1 ps pulses.

# Chapter 2

## How to shorten 1 ps pulses

This chapter gives an overview of different pulse shortening techniques conducted in optical fiber or bulk. As the aim of this work is to shorten 1 ps pulses, their suitability for this pulse duration is discussed.

In general, extracavity pulse shortening consists of two stages. First the narrow-band input pulse is sent to fiber or bulk where it undergoes spectral broadening. In the second stage the hereby acquired chirp is compensated by dispersive optical elements like chirped mirrors or gratings to temporally compress the pulse. Because the interest of this thesis focuses on nonlinear effects, the underlying physical principles of dispersive elements are not discussed in detail.

### 2.1 Large mode area fibers

In contrast to conventional optical fibers consisting of two concentric glass cylinders with different refractive indices, photonic crystal fibers (PCF) are made from a single material (usually silica). The light guidance happens in the either hollow or solid core of the fiber. In the case of large mode area (LMA) fibers, the cross-section of the fiber shows a hexagonal honeycomb pattern of air holes running along the length of the crystal as shown in Fig. 2.1. The missing center hole enables a silica defect which makes up the solid core [25]. More geometrical degrees of freedom in comparison to conventional optical fibers enable waveguide engineering in LMA fibers. By changing the size of the air holes and their periodicity, the zero dispersion wavelength can be tuned [26] and the region of single-mode guidance can be extended from the UV to the MIR [27]. The larger effective mode area helps to increase the optical damage threshold and scale the input average power to regimes not reachable with conventional fibers [28].

The broadening mechanisms occurring during pulse propagation in the fiber differ from normal to anomalous dispersion. In the regime of normal dispersion, spectral broadening is caused by Raman scattering, self-phase modulation and, various four wave mixing processes. For anomalous dispersion soliton-related dynamics dominate [29].

For 100 fs input pulses ultrabroadband continua extending from 390 to 1600 nm could be generated [30]. Their spectral shape is flat and therefore allows good temporal compression. Simulations showed that spectral coherence and stability depend on the input pulse duration

[31]. Nicholson et al. [32] experimentally compared continua generated by 188 fs and 2 ps pulses. For input pulses in the picosecond range the spectra showed almost no coherence although the initial pulses were highly coherent. This means that the LMA output spectra show high shot-to-shot instability when generated from pulses with picosecond duration. Shot-to-shot instability of the OPA seed causes undesirable energy fluctuations of the amplified pulse. This quality degradation limits the application of LMA fibers to pulses with femtosecond duration.

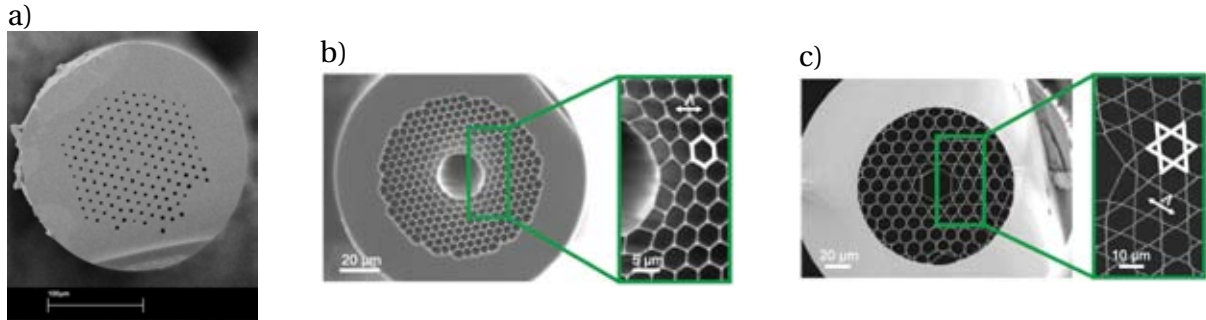


**Figure 2.1:** Different types of photonic crystal fiber. a) Scanning electronmicroscope (SEM) image of a large mode area fiber. Adapted from: "Nonlinear femtosecond pulse compression at high average power levels by use of a large-mode-area holey fiber", by T.Suedmayer et al., 2003, Opt. Lett., 28, p. 1952. b) SEM image of a photonic bandgap guiding HCF. c) SEM image of a Kagomé-type HCF. Adapted from: "Ultrafast nonlinear optics in gas-filled hollow-core photonic crystal fibers", by J. C. Travers et al., 2011, J. Opt. Soc. Am. B, 28, p. 12.

## 2.2 Hollow core fibers

Although solid core PCFs offer the advantage of high nonlinearity at low losses and a predictable dispersion [33], their limitation in input power led to the development of another spectral broadening technique based on gas-filled hollow core fibers (HCF). The hollow core is surrounded by a hexagonal cladding made of fused silica to confine the light by the two-dimensional photonic bandgap-effect. A sufficient fiber length guarantees single-mode propagation while suppressing higher order modes. Noble gas filling ensures both a high threshold intensity for multiphoton ionization and the tunability of the nonlinearity strength by changing the gas type and gas pressure [34]. The larger mode diameter can increase the damage threshold and enable input pulse energies in the sub-mJ range [35]. By using chirped pulses to lower the optical intensity and avoid gas ionization, Bohman et al. [36] achieved spectral broadening for 5 mJ pulses. Differentially pumped HCFs, where a vacuum is maintained at the entrance of the fiber, reach higher transmission efficiency and more spectral broadening than statically filled HCFs because ionization defocusing is reduced [37]. Besides the common hexagonal structured HCFs, Kagomé-type HCFs with a star-of-David patterned cladding can be used. Here the light guidance is provided by the inhibited coupling between the core and the cladding modes [38]. Therefore Kagomé fibers offer a broader transmission range at lower losses [33].

Kagomé HCFs also offer the possibility of self-compression instead of conventional pulse shortening with spectral broadening followed by dispersion compensation. The group velocity dispersion becomes anomalous at lower gas pressures because of the smaller core area [39]. This leads to a soliton-effect pulse compression where the anomalous dispersion balances the chirp induced by self phase modulation. Mak et al. [40] achieved compression of 1- $\mu$ J, 250-fs pulses from a thin-disk oscillator to sub 10-fs pulses with an average power of 14.5 W at 38 MHz repetition rate in a two-stage Kagomé-HCF system. The first stage utilized SPM spectral broadening and chirped mirror compression, whereas the second stage operated in the anomalous dispersion regime where the pulse undergoes soliton-effect self-compression.

Voronin et al. [38] simulated the compression of 1-ps pulses in a system of cascaded gas-filled HCFs with dispersion-control. Their results and the experimental results of Heckl et al. [41] showed that the compression of pulses with a duration of 1 ps is feasible with hollow core fiber technology. To quantify the quality of pulse compression both groups calculated the quality factor  $Q$ , which is the ratio of the energy contained in the main peak and the total pulse energy. The fact that  $Q$  achieved a maximum value of 63 % in simulation and 60 % in experiment demonstrates the limitation of HCF-technology to pulses with femtosecond duration. For increasing pulse duration higher order dispersion and discontinuities in the spectral phase lead to imperfect pulse compression. This is expressed in the form of strong side pulses and long pedestals.

## 2.3 Spectral broadening in bulk

Spectral broadening in bulk can occur due to two different processes. The less complex process of self-phase modulation includes only temporal dynamics. Due to the intensity dependence of the nonlinear refractive index the temporally varying intensity of the pulse causes a phase shift and modifies the instantaneous frequency of the electric field of the pulse [42]. This leads to the generation of new frequencies and therefor to spectral broadening.

The more complex process of supercontinuum generation involves the coupling of spatial and temporal effects [29]. This phenomenon is expressed by the generation of an extremely broadband pedestal on the blue side of the spectrum. It is observed when the input power exceeds the critical power for self-focusing in matter. The reason for supercontinuum generation is the formation of an optical shock wave at the back of the pulse due to focusing in space and time as well as self-steepening [43].

The practical advantages of spectral broadening in bulk towards spectral broadening in optical fibers cannot be denied. Setups become more compact and easier to handle without employing noble gases and meter-long beam passes. The nonlinear refractive index  $n_2$  in solids is 1000 times larger than in gases [24], allowing the interaction length to be kept short. Besides the experimental advantage of less alignment-sensitivity broadening in bulk crystals can reduce intensity fluctuations observed in gas-filled Kagomé-HCFs [44]. At the same time multiple filamentation and optical damage sets in if the pulse energy exceeds a few  $\mu$ J [45]. Another issue is the large material dispersion which the pulse experiences while propagating through the medium [46]. In the 1980s, when spectral broadening in bulk first came up, it enabled higher input energies than the step-index fibers commonly used at that time [47].

But the development of LMA fibers and later HCF fibers led to the domination of spectral broadening by fiber technology.

Due to the undeniable experimental advantages of bulk crystals towards gas-filled HCFs, there was always interest in improving the performance of spectral broadening in bulk. The commonly used material for continuum generation is sapphire [48]. The use of laser host materials like Yttrium Aluminum Garnet (YAG) and Yttrium Vanadate ((YVO)<sub>4</sub>) can extend the generated continuum to the MIR and decrease the input energy needed to start supercontinuum generation [49]. By focusing 85-fs, 6.9  $\mu$ J pulses in YAG crystal, Silva et al.[50] could generate a carrier-envelope-phase stable spectrum spanning from 450 nm to 4.5  $\mu$ m. Their simulations predict a pulse duration reduction by more than a factor of 10 due to self-compression in filamentation [51].

A setup consisting of multiple thin fused silica plates proposed by Lu et al. [24] allows for input energies in the same regime as reported for HCFs. Limiting the plate thickness causes the pulse to exit the medium after spectral extension, but before multiple filamentation and optical damage sets in. While propagating in air, the pulse can refocus in space and recompress in time. Employing four plates, a spectrum spanning from 450 to 980 nm with 54 % conversion efficiency could be achieved from 25 fs input pulses with 140  $\mu$ J pulse energy.

Spectral broadening in bulk for pulse durations in the few hundred fs regime is a well-established technique. If the input pulse duration is increased to 1 ps the damage threshold of the bulk material becomes one of the limiting factors. The crystal gets locally damaged by the increased exposure time and energy content which becomes necessary to reach sufficient intensities for 1 ps pulses [52]. Therefore it is hard to find a suitable material for spectral broadening in bulk with 1 ps input pulses.

## 2.4 Summary and conclusion

Three different techniques for spectral broadening were introduced: spectral broadening in LMA, HCF and bulk. In fiber technology, the broadening mechanism can be explained by purely temporal dynamics namely SPM, Raman scattering and four-wave mixing. In LMA the nonlinear interaction takes place in a silica core whereas in HCFs gases are employed. A solid core offers the advantage of high nonlinearity, predictable dispersion, and less fluctuation. Gases however allow for higher input energies and less losses in connection with enhanced guidance mechanisms. Although HCFs are widely spread today, their alignment sensitivity, high susceptibility to damage, and complexity make the use of bulk crystals more attractive from the experimentalist's point of view. Supercontinuum generation in bulk is a complex process involving a coupling between spatial and temporal effects. Easy handling, simplicity, and cost effectiveness of bulk setups come at the cost of decreased input energies due to multiple filamentation and material damage. The multiple thin plate approach proposed by Lu et al. [24] seems to be a promising way to catch up with the performance of HFCs. Since high input energy is not as critical in seed generation for OPAs as it is in pulse compression for high power lasers the multiple thin plate approach is an interesting alternative for our applications.

When it comes to the applicability to 1 ps pulses, all three methods show major drawbacks. To reach a stable, coherent, and well-compressible continuum the demand for a suitable pre-compression stage appears. To fulfill this demand we conducted experimental as well as nu-

merical studies on two independent techniques that allow pulse shortening from 1 ps to a few hundred femtoseconds.

# Chapter 3

## Cross Polarized Wave Generation

When the process of cross polarized wave generation (XPW) was first observed experimentally, it was predicted to become an important tool to measure the nonlinear susceptibility of crystals with high accuracy [53]. Later XPW was used to implement temporal filters to enhance the contrast ratio of femtosecond pulses by more than four orders of magnitude [54, 55]. Although this is nowadays the main application, the XPW process has some features that have been largely neglected. This thesis presents an approach that takes advantage of the pulse duration reduction and spectral broadening [56] occurring during XPW.

The following chapter explains the theoretical background of the underlying nonlinear effect and the cascaded setup used to shorten 1-ps pulses down to less than 250 fs. The experimental and numerical results are discussed and the influence of different third-order nonlinearities and the spectral phase is illuminated.

### 3.1 Basic understanding of the process

While propagating through a nonlinear crystal, intense light pulses experience nonlinear polarization rotation and induced ellipticity (XPW). Both are third-order nonlinear processes whereof nonlinear polarization rotation is proportional to the imaginary part and XPW to the real part of the  $\chi^{(3)}$  anisotropy [57]. During the XPW process part of a linearly polarized incident wave is converted to a wave with orthogonal polarization with respect to the input wave at the same wavelength[58], as depicted in Fig. 3.1. This process is classified as a degenerate four-wave mixing process and is therefore automatically phase matched. During the XPW process, the carrier envelope phase is preserved [59]. The intensity of the generated wave is proportional to the cube of the intensity of the incident wave. That leads to temporal contrast enhancement [60], because the pedestal and side pulses with lower intensity compared to the main pulse are suppressed. In frequency domain temporal filtering translates into a smoother spectrum. Besides temporal cleaning, the process also acts as a spatial filter [61].

Starting from Maxwell's equations, one can derive the nonlinear wave propagation equation

$$\Delta \vec{\mathcal{E}} - \frac{n^2}{c^2} \frac{\partial^2 \vec{\mathcal{E}}}{\partial t^2} = \mu_0 \frac{\partial^2 \vec{P}^{NL}}{\partial t^2}, \quad (3.1)$$

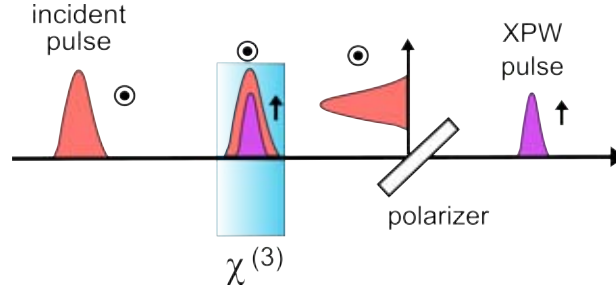


**Figure 3.1:** Scheme of the XPW process: An intense, linearly polarized pulse generates a pulse with orthogonal polarization in a crystal with  $\chi^{(3)}$  anisotropy. Incident and generated pulse can be separated with a polarizer.

where  $\vec{\mathcal{E}}$  is the electric field,  $n$  the refractive index,  $c$  the speed of light,  $\mu_0$  the vacuum permeability, and  $\vec{P}^{NL}$  the nonlinear dielectric polarization. The latter reduces to  $\vec{P}^{NL} = \epsilon_0 \chi^{(3)} \vec{\mathcal{E}} \vec{\mathcal{E}} \vec{\mathcal{E}}$  if only the third-order susceptibility tensor  $\chi^{(3)}$  is considered. In general,  $\chi^{(3)}$  is a fourth-rank tensor containing 81 elements, but due to crystal symmetry most of them vanish.

Using the slowly varying amplitude approximation and omitting the terms that belong to third harmonic generation, Eq. 3.1 yields the following system of differential equations:

$$\begin{aligned} \frac{dA}{d\zeta} &= i\gamma_1 AAA^* + i\gamma_2 AAB^* + 2i\gamma_2 ABA^* + 2i\gamma_3 ABB^* + i\gamma_3 BBA^* + 2i\gamma_4 ABB^*, \\ \frac{dB}{d\zeta} &= i\gamma_5 BBB^* + i\gamma_4 BBA^* + 2i\gamma_4 ABB^* + 2i\gamma_3 ABA^* + i\gamma_3 AAB^* + i\gamma_2 AAA^*. \end{aligned} \quad (3.2)$$

$A$  is the complex amplitude of the incident wave and  $B$  is the complex amplitude of the generated wave,  $\zeta$  is the propagation direction and  $\gamma_i$  are coefficients depending on the crystal orientation, and the components of  $\chi^{(3)}$ .

All  $\gamma$ -coefficients can be referred to different third-order nonlinear processes [62].  $\gamma_1$  and  $\gamma_5$  are responsible for self-phase modulation (SPM),  $\gamma_3$  for cross-phase modulation (XPM) and  $\gamma_2$ , and  $\gamma_4$  for cross-polarized wave generation.

The temporal shape during the process stays unchanged, but the pulse duration is reduced by a factor of  $\sqrt{3}$  [56]. Also for modulated input spectra the XPW spectrum has a Gaussian shape and is broadened by a factor of  $\sqrt{3}$  [63].

### Crystal of choice: material and orientation

In principal, all crystals with an anisotropic  $\chi^{(3)}$  tensor are suitable for XPW. To assure perfect group-velocity matching between the incident and the generated cross-polarized wave, the crystal has to be cubic. To avoid two-photon absorption, the band gap has to be larger than 4 eV in the case of  $1 \mu\text{m}$  input pulses. As the conversion efficiency of XPW is proportional to the anisotropy of the  $\chi^{(3)}$  tensor, a crystal with high  $\chi^{(3)}$  anisotropy is preferable.  $\text{BaF}_2$ ,  $\text{CaF}_2$  and  $\text{LiF}$  fulfill these requirements but only  $\text{BaF}_2$  has a broadband transmission range from 0.2 to  $11 \mu\text{m}$  [60, 62].

Besides the chemical properties, the crystal orientation is an important parameter to maximize the conversion efficiency. At first, crystals with [001]-cut were used and a maximal conversion efficiency of 11 % was achieved [64]. At high input energies the efficiency saturates because of the induced phase mismatch due to SPM and XPM. Using [011]-cut (holographic cut) crystals can avoid this phenomenon and the conversion efficiency can be further increased. Fig. 3.2 compares the calculated conversion efficiency of a [001]-cut (Fig. 3.2 -a) and a [011]-cut (Fig. 3.2 -b) crystal for different phase matching angles  $\beta$ . Another advantage of the holographic cut is the decreased sensitivity to the orientation of the incident polarization [65].

Following these considerations all crystals used in the experiment were holographic cut BaF<sub>2</sub> crystals.

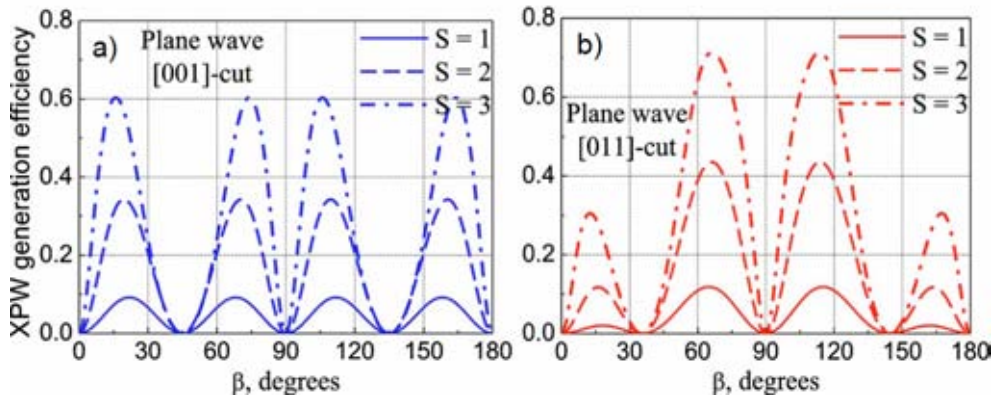


**Figure 3.2:** Calculated conversion efficiency of the XPW process as a function of the phase matching angle  $\beta$  for different normalized input intensities  $I_0$  and  $S = \gamma_0 L I_0$ . a) shows the development for a [001]-cut crystal and b) for a [011]-cut crystal. The high values for the efficiency are caused by using plane waves instead of a Gaussian beam. Adapted from: "Efficient generation of cross-polarized femtosecond pulses in cubic crystals with holographic cut orientation.", by L. Canova et al., 2008, Appl. Phys. Lett., 92, p. 1.

## Maximizing conversion efficiency

The conversion efficiency  $\eta$  of the XPW process is governed by three experimental parameters: the phase matching angle  $\beta$ , the input intensity  $I_0$ , and the crystal length  $L$ [54]:

$$\eta = (\gamma_{\perp} I_0 L)^2. \quad (3.3)$$

The coefficient  $\gamma_{\perp}$  depends on the anisotropy of the  $\chi^{(3)}$  tensor and on  $\sin(4\beta)$ . Rotating the crystal around the optical axis changes  $\beta$ . Fig. 3.2 shows that for [011]-cut crystals the conversion efficiency reaches two maxima at 70 and 110 degrees. The high value of the conversion efficiency is caused by the fact that the calculations were done for plane waves. For a wave with Gaussian characteristics in space and time the value reduces by nearly a factor of 6 [54].

Experimentally  $\beta$  is the easiest parameter to optimize by rotating the crystal until the generated XPW signal reaches its maximum. Readjusting  $\beta$  to compensate for intensity dependent phase mismatch is not required in the case of [011]-cut crystals [65].

In contrast, the input intensity is experimentally restricted by the optical damage threshold of the crystal. In Fig. 3.3 -a the simulated conversion efficiency of the XPW process is depicted as a function of the input peak intensity for a pulse with Gaussian characteristics in space and time. For more details on the simulation see Appendix B. In agreement with equation 3.3 the conversion efficiency grows with the square of the input peak intensity as the fitted solid line shows. For different crystal thicknesses the conversion efficiency saturates at certain values and evolves away from the quadratic fit. For a 2 mm thick crystal saturation is not reached within  $1.5 \text{ TW/cm}^2$  input peak intensity. In the limit of high intensities equation 3.3 is no longer valid and the conversion efficiency converges to a constant value which only depends on the anisotropy of the  $\chi^{(3)}$  tensor [58]. Fig. 3.3 -b shows the measured conversion efficiency as a function of the input power for a Gaussian pulse focused with a convex lens with 750 mm focal length. The three crystals of different length were placed 30 mm behind the focal spot. The input power was increased up to the damage threshold for each crystal. The quadratic fit (solid line) of the data points proves the agreement with equation 3.3. Experimentally the saturation regime cannot be reached because the damage threshold of the crystals is too low.

We measured the immediate optical damage threshold for a 4 mm and a 6 mm  $\text{BaF}_2$  crystal. The crystals were placed at the focus of a 750 mm convex lens to reach a beam size of  $70 \mu\text{m}$  (FWHM) on the crystal. The input energy was increased gradually until we saw a bright spot on the crystal surface and the transmitted energy dropped. For the 6 mm crystal we calculated a peak intensity of  $525 \pm 92 \text{ GW/cm}^2$  and for the 4 mm crystal a peak intensity of  $908 \pm 151 \text{ GW/cm}^2$ . The large measurement error is caused by the high inaccuracy in determining the exact beam size and the energy at which the damage sets in. The lower damage threshold for the 6 mm crystal is caused by self-focusing in the crystal, which occurred before the crystal surface got damaged.

The third experimental parameter to be optimized is the crystal length. Jullien et al. [66] showed that for 45 fs pulses the conversion efficiency of XPW in a 2 mm and a 6 mm  $\text{BaF}_2$  crystal saturates at the same value. This saturation limit for long crystals is caused by a decrease in the spatial overlap between the incident and the generated beam due to SPM and by the occurring continuum generation after self-focusing. For pulses with a pulse duration below 100 fs also dispersion plays a major role. In long crystals dispersion chirps the input pulse and causes a reduction of the spectral broadening happening during the XPW process [63]. To avoid these effects Jullien et al. suggested a two crystal arrangement that achieves higher conversion efficiency than a single crystal of the same length. In the two crystal arrangement the pulse exits the first crystal before it undergoes SPM and the intensity on the second crystal is increased due to the Kerr lens effect. In agreement with their findings Fig. 3.3 -a shows that for 1 ps pulses XPW in a 6 mm and a 4 mm  $\text{BaF}_2$  crystal reaches saturation at the same value. However, when considering pulses longer than a few hundred fs dispersion is negligible and

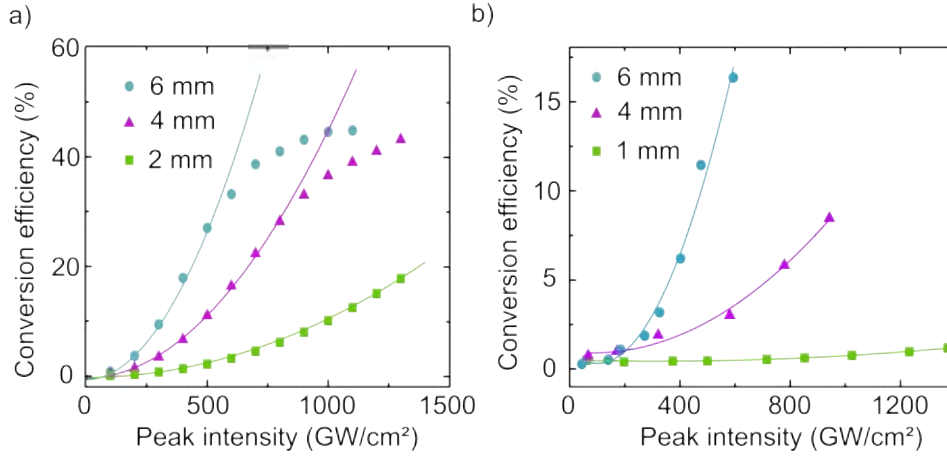


**Figure 3.3:** Simulated (a) and measured (b) conversion efficiency of XPW as a function of the input peak intensity for different crystals of different length. The solid lines show a quadratic fit of the data points before saturation sets in.

the damage threshold of the material becomes the main limiting factor because it is inversely proportional to the square of the pulse duration [67]. As Fig. 3.3 -b shows out of saturation regime longer crystals reach higher conversion efficiency at lower input power. Therefore in experiment longer crystals are preferred because operation close to saturation regime is impossible due to the reduced damage threshold for 1 ps pulses.

To allow for higher input intensities a two crystal arrangement could still be beneficial. With two shorter crystals self-focusing can be avoided, because the pulse exits the crystal before self-focusing occurs. In this way the damage threshold can be increased. However, to keep the setup as simple as possible it was never implemented.

Another method to fight self focusing is to change the divergence of the beam by using lenses with different focal length. Therefore the beam was focused with four convex lenses with  $f=125$  mm,  $f=200$  mm,  $f=500$  mm, and  $f=750$  mm keeping the distance between the crystal and the focal spot constant. The results are represented in Fig. 3.4. The weakest lens achieves the highest conversion efficiency. For the lens with  $f=750$  mm beam divergence balances self-focusing. Stronger focusing leads to a more divergent beam and therefore to an intensity reduction on the crystal.

Taking all these considerations into account, the setup of choice consists of a convex lens with  $f=750$  mm and a  $\text{BaF}_2$  crystal with holographic cut and a length of 6 mm. At an input peak intensity of  $400 \text{ GW/cm}^2$  the XPW conversion efficiency reaches values higher than 10%. However after 5 to 10 minutes operation at this peak intensity a bright spot on the crystal appears and the XPW signal drops. For long term operation the input peak intensity has to be reduced to a maximum of  $330 \text{ GW/cm}^2$ . The discrepancy between the measured immediate optical damage threshold and this value is caused by thermal processes that occur after heating up the crystal.  $330 \text{ GW/cm}^2$  peak intensity corresponds to a pulse energy of  $210 \mu\text{J}$ . With

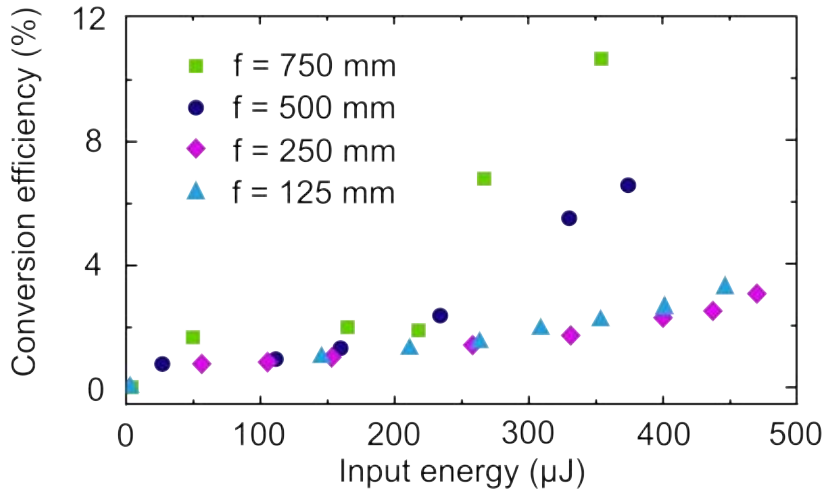


**Figure 3.4:** Dependence of the XPW conversion efficiency on the beam divergence: The distance between the crystal and the focal spot was kept constant for all lenses.

the generated 18  $\mu\text{J}$  of XPW energy we end up with a conversion efficiency of 9 %.

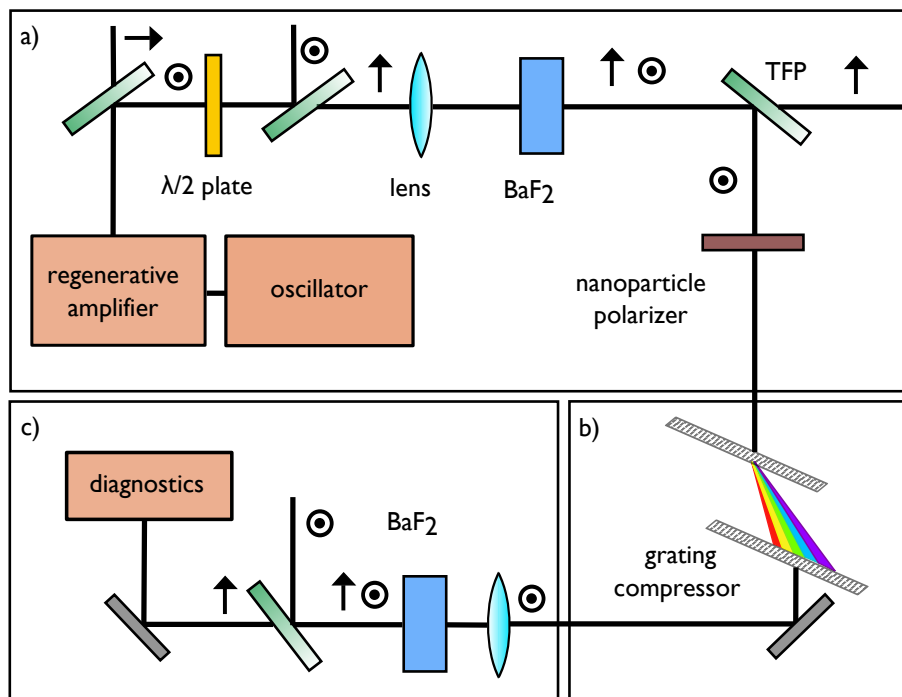
## 3.2 Experimental setup for cascaded XPW

Knowing about the benefits of XPW, we designed a very simple setup that is capable of pulse shortening and spectral broadening by a factor of 3. The basic idea is to use a cascade of  $\text{BaF}_2$  crystals and filter out the incident pulse after each crystal.

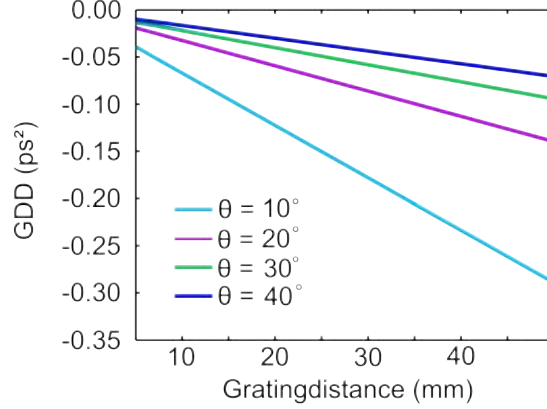
The experimental setup for cascaded XPW consists of two stages with a similar architecture. The source for the 1-ps Gaussian input pulses centered at 1030 nm is an all Yb:YAG regenerative thin-disk amplifier seeded by a Kerr-lens mode-locked Yb:YAG thin-disk oscillator. The system delivers an average power of 130 W at a repetition rate of 5 kHz which corresponds to a pulse energy of 26 mJ. For more detail see [18].

Fig. 3.5-a shows the first stage of the XPW setup. A fraction of the output of the regenerative amplifier (5 W) is sent to a first thin film polarizer (TFP) with  $T_P > 95\%$ . Only the reflected s-polarized part of the beam (3 W) is used. An attenuator built from a  $\lambda/2$ -plate and a second TFP with  $T_P > 98\%$  enables the scalability of the input power. These components allow for a p-polarized pulse with less than 0.1 % s-polarization tunable from 0-500  $\mu\text{J}$ . A convex lens with  $f = 750$  mm focuses the beam to a 6 mm [011]-cut  $\text{BaF}_2$  crystal. The crystal is placed about 30 mm behind the focus yielding a beam size of 260  $\mu\text{m}$  ( $D_{FWHM}$ ) on the crystal surface. Another TFP with  $T_P > 98\%$  is employed to separate the s-polarized XPW and the p-polarized input pulse. A nanoparticle linear film polarizer absorbs the remaining p-polarized components in the reflected s-polarized path to increase the total extinction ratio.

Fig. 3.5-b shows a compression stage consisting of a pair of transmission gratings (Light



**Figure 3.5:** XPW setup: a) First XPW stage: The linearly polarized input pulse is focused to a 6 mm  $\text{BaF}_2$  crystal where the XPW signal is generated. To separate pump and XPW pulse a TFP is employed. b) Compression stage: A grating compressor compensates for the chirp acquired during the XPW process. c) Second XPW stage: The nearly FT limited pulse is focused to a second 6 mm  $\text{BaF}_2$  crystal. Another TFP is employed to separate the generated and the incident pulse.



**Figure 3.6:** Calculated GDD of a pair of transmission gratings with groove density  $1000 \text{ mm}^{-1}$  as a function of the grating distance at different incident angles  $\theta$ .

Smith, LSF-1000) with a groove density of  $1000 \text{ mm}^{-1}$  in single-pass configuration. The single-pass configuration is preferred to keep the setup simple and avoid additional optical components. Spatial separation of the spectral components can be neglected due to the narrow spectral width. The compression stage is optional and operated to compensate the chirp of the XPW pulse after the first stage. The group delay dispersion (GDD) introduced by the gratings is calculated according to [68]:

$$GDD = -\frac{d \cos \theta \lambda}{2\pi c^2} \left( \frac{\lambda N}{\cos \beta} \right)^2, \quad (3.4)$$

where  $d$  is the grating distance,  $\beta$  the diffraction angle,  $\lambda$  the wavelength,  $c$  the speed of light and  $N$  the groove density. Eq. 3.4 is valid if the angle between the propagation of the center wavelength and the outer wavelength is small. In the case of a narrow-band input this assumption holds.

For an incident angle of  $\theta = 30^\circ$  the first diffraction order is maximized. From Fig. 3.6 the grating distance to achieve the desired value of GDD at this incident angle can be identified. The measured transmission efficiency of the grating pair is higher than 92 % in single-pass configuration.

Fig. 3.5-c shows the second XPW stage. The XPW signal generated in the first XPW stage is focused to another 6 mm  $\text{BaF}_2$  crystal placed 5 mm behind the focus of a convex lens with  $f = 100 \text{ mm}$ . Similar to the first stage a TFP with  $T_p > 98\%$  is employed to separate the generated from the incident pulse. Additional polarization cleaning is not needed because the XPW signal is now the transmitted p-polarized part. Tighter focusing in comparison to the first stage is necessary to reach sufficient peak intensities on the second crystal because the incident pulse energy is limited to  $18 \mu\text{J}$ . The beam size on the crystal was  $140 \mu\text{m}$  which corresponds to a peak intensity of  $150 \text{ GW/cm}^2$ . This value is still more than a factor of 2 smaller than the peak intensity reached on the first crystal. However further reduction of the beam size on the crystal by using a lens with shorter focal length does not increase the conversion

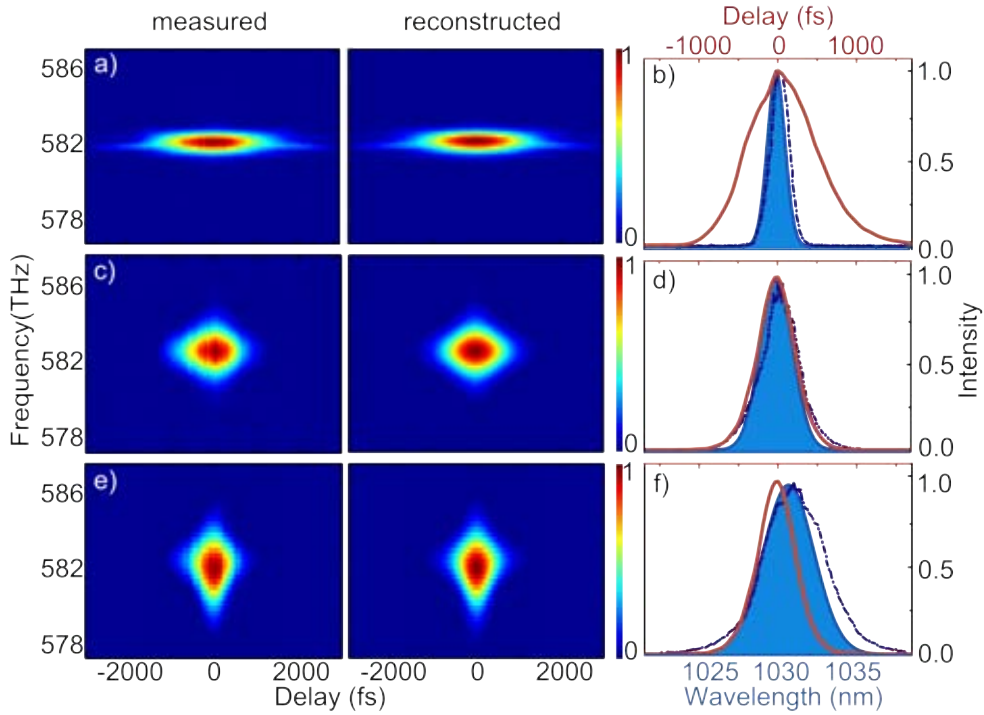


**Figure 3.7:** Input pulse and XPW pulse after each stage: a), c) and e) Measured and reconstructed SHG-FROG trace.  $G_{error}: 2.8 \times 10^{-3}$ ,  $G_{error}: 5.9 \times 10^{-3}$  and  $G_{error}: 5.0 \times 10^{-3}$ , respectively. b), d) and f) Retrieved temporal profiles (red line), retrieved (solid blue line) and measured (dashed blue line) spectra.

efficiency of the XPW process. As discussed in the previous section, a more divergent beam leads to a lower conversion efficiency. In this setup the maximal conversion efficiency of the second stage is 3.5 %. With a conversion efficiency of 8.5 % in the first stage the total conversion efficiency of the cascaded XPW is 0.3 %.

### 3.3 Experimental results

To proof the performance of the XPW system measurements without compression between first and second XPW stage were conducted. Frequency resolved optical gating based on second harmonic generation (SHG-FROG) employing a 100  $\mu\text{m}$  thick BBO crystal was used to characterize the pulses before and after each stage. For more details on the working principle of this measurement technique see Appendix A. To prove the FROG results the according spectra were measured using an Ocean Optics HR 4000 spectrometer.

Fig. 3.7 -a, -c and -e, respectively, depict the measured and reconstructed spectrograms of the input pulse, the XPW pulse after the first stage and the XPW pulse after the second stage. Without retrieving it can be seen from the spectrograms that the XPW signal is self-compressed and spectrally broadened after each stage. The retrieved time-envelopes (solid red line) and spectra (blue area) in Fig. 3.7 -b, -d and -f confirm this assumption. The good

agreement of the measured spectra (slashed blue line) and the reconstructed spectra as well as the  $G_{error}$  below  $6 \times 10^{-3}$  are an indicator for the high quality of the measurements. Although the time-envelope of the input pulse is asymmetric and inhomogenous, the XPW signals are perfect Gaussian pulses and their spectra have a Gaussian shape. This quality enhancement is a beneficial side-effect of the XPW process.

**Table 3.1:** Pulse energy, pulse duration and spectral width of the input pulse and the XPW pulse after each stage.

|             | pulse energy      | pulse duration | spectral width |
|-------------|-------------------|----------------|----------------|
| input pulse | 210 $\mu\text{J}$ | 1 ps           | 1.6 nm         |
| XPW 1       | 18 $\mu\text{J}$  | 537 fs         | 3.0 nm         |
| XPW 2       | 0.5 $\mu\text{J}$ | 326 fs         | 4.4 nm         |

In Tab. 3.1 all parameters retrieved from the FROG measurement and the recorded pulse energy are listed. The values for pulse duration and spectral width indicate the full width half maximum (FWHM) of the curves in Fig. 3.7. The pulse is shortened from 1 ps to 537 fs in the first stage and 326 fs in the second stage. Spectral broadening from 1.6 nm to 3.0 nm and 4.4 nm is observed. To compare the parameters to theory a factor to quantify the pulse shortening  $F_\tau$  and spectral broadening  $F_{\Delta\lambda}$  was calculated:

$$F_\tau = \frac{\text{pulse duration before XPW}}{\text{pulse duration after XPW}}$$

$$F_{\Delta\lambda} = \frac{\text{spectral width after XPW}}{\text{spectral width before XPW}}$$

According to theory,  $F_\tau$  and  $F_{\Delta\lambda}$  are equal to  $\sqrt{3} \approx 1.7$ . For the first XPW stage  $F_\tau$  and  $F_{\Delta\lambda}$  take the value 1.9 which is higher than the expected theory value. In contrast, for the second stage  $F_\tau$  is 1.6 and  $F_{\Delta\lambda}$  is 1.5 which is smaller than the expected theory value. Why we see this contrary deviation from theory in both stages will be discussed in the following sections.

### 3.3.1 Influence of different third-order nonlinearities

Since the second XPW stage operates on the output of the first XPW stage, we first need to understand why we see an upward deviation from theory in the first stage to analyze the downward deviation in the second stage. To identify if  $F_\tau$  and  $F_{\Delta\lambda}$  depend on conversion efficiency, we ran the first XPW stage for different input energies ranging from 80 to 260  $\mu\text{J}$  and measured FROG-traces with and without the compression stage. For all energies the spectra with and without compression were also recorded with the spectrometer. Besides the experiment, we simulated the XPW process for different peak intensities to reach comparable conversion efficiency.

Fig. 3.8 -a shows the evolution of the spectral width  $\Delta\lambda_{FWHM}$  for increasing conversion efficiency. The values retrieved from the FROG measurements with (blue dots) and without compression (red stars) are in agreement as well as the simulated (green triangles) and measured values (blue diamonds). Between the pairs is a constant discrepancy of 0.5 nm. However all values show the same behavior. For conversion efficiency smaller than 4 % all values

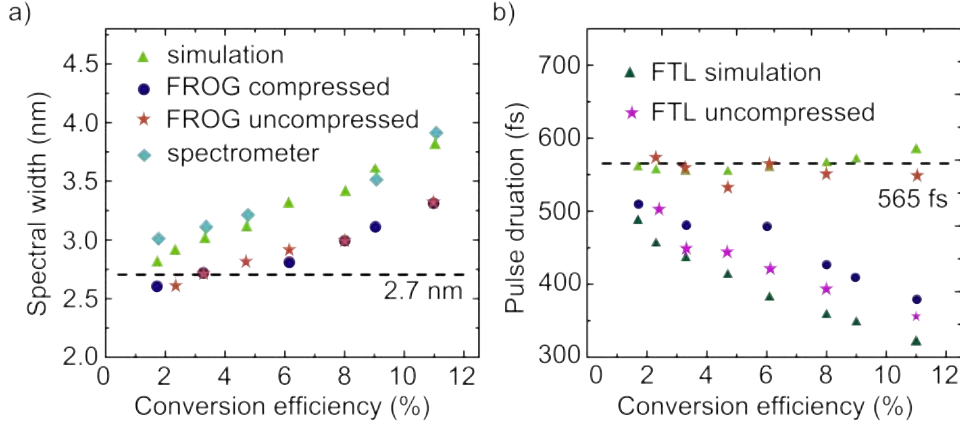


**Figure 3.8:** Influence of conversion efficiency on spectral width and pulse duration: a) Full width half maximum of the spectra from different measurements and simulation. The dashed black line shows the theory value calculated by multiplying the input spectral width by  $\sqrt{3}$ . b) According pulse duration and FT limit. The dashed black line shows the theory value for the pulse duration.

are close to the theory value of 2.7 nm (input spectral width  $\times \sqrt{3}$ ). For higher conversion efficiency they increase almost linearly up to 3.9 nm and 3.6 nm, respectively, which corresponds to  $F_{\Delta\lambda} = 2.4$  and  $F_{\Delta\lambda} = 2.3$ .

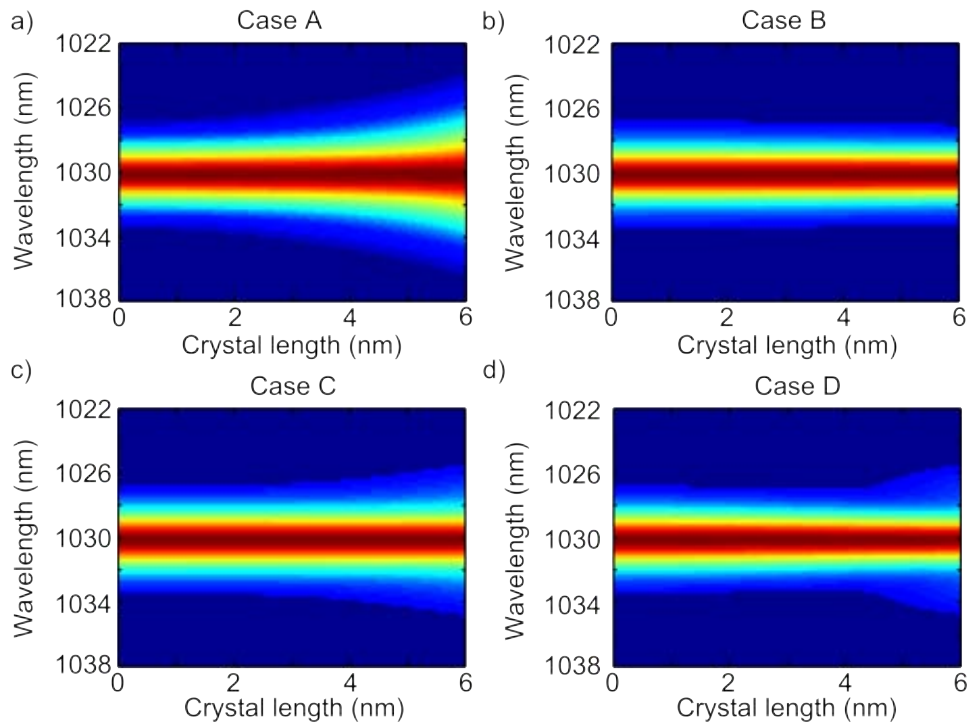
Fig. 3.8 -b shows the evolution of the pulse duration  $\tau_{FWHM}$  and the FT limit. In contrast to the spectral width the pulse duration retrieved from the uncompressed FROG measurement and from simulation are nearly constant and stay close to the theory value of 565 fs for all conversion efficiencies. The FT limit of the simulation and the uncompressed measurement decrease. As an indicator for the good performance of the transmission gratings the compressed pulse duration is in agreement with the FT limit of the uncompressed measurement. The constant discrepancy between the FT limit of simulation and experiment is a consequence of the broader spectrum achieved in simulation. Both values are connected by the minimum time-bandwidth-product which is  $0.44 = \tau_{FWHM} \cdot \Delta\omega_{FWHM}$  in the case of a Gaussian pulse. The discrepancy in the spectral width might be caused by the FROG-retrieval algorithm because simulation and spectrometer as well as simulation and pulse duration agree.

Fig. 3.8 shows that with increasing conversion efficiency we see an additional spectral broadening to the spectral broadening caused by XPW. Although the spectrum gets broader the pulse duration does not reduce which indicates that induced spectral phase causes higher order dispersion. Since XPW is thought to be a self-compressed process, other nonlinear effects that are enabled by higher intensities must be responsible for the described phenomenon.

### Simulating different third-order nonlinearities

While simulating the XPW process, Eq. 3.2 is solved in a split-step method. As mentioned above, the different  $\gamma$ -coefficients are responsible for SPM, XPM and XPW. To analyze the influence of each nonlinearity individually, we simulated the process for four different cases:

- Case A: all effects included,



**Figure 3.9:** Influence of different third-order effects: a), b), c) and d) show the simulated evolution of the XPW spectrum while propagating along the crystal for four different cases mentioned in the main text.

- Case B: only XPW included,
- Case C: XPW and SPM include, and
- Case D: XPW and XPM included

by setting the according  $\gamma$ -coefficient to zero.

Fig. 3.9 shows the resulting XPW spectra while propagating along a 6 mm BaF<sub>2</sub> crystal for case A to D. Up to a crystal length of 2 mm all four spectra behave similarly. The spectral width stays constant and agrees with the theory value of 2.7 nm. For longer crystal length the spectrum in Case A is the first one to start additional broadening. The spectrum broadens homogenously and reaches a spectral width (FWHM) of 4.5 nm at the end of the crystal. This behavior is in good agreement with the experimental observations. In Case C the spectrum starts broadening after 3 mm but only the wings become broader. At the end of the crystal the full width half maximum of 2.8 nm is very close to the value at the beginning. By setting  $\gamma_3$  (responsible for XPM) and  $\gamma_1$  (responsible for SPM of the incident pulse) or  $\gamma_3$  and  $\gamma_5$  (responsible for SPM of the XPW pulse), respectively, to zero we could identify that this effect occurs due to SPM of the XPW pulse. SPM of the incident pulse does not affect the XPW spectrum. The spectrum in Case D starts broadening after 4 mm. The wings of the spectrum broaden but the central part even experiences spectral narrowing to end up with a full width half maximum of 2.4 nm. In Case B the spectrum stays constant all throughout the crystal. We repeated all simulations without taking dispersion and diffraction into account and achieved

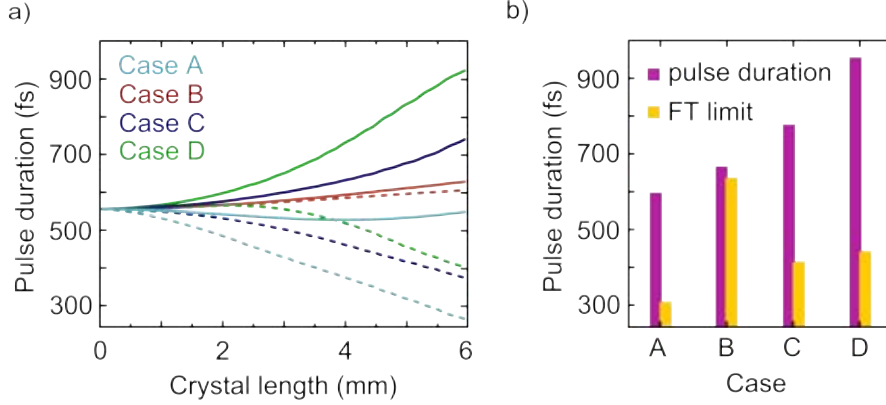


**Figure 3.10:** a) Simulated evolution of the pulse duration and the FT limit for Case A to D while propagating along the crystal. b) Illustration of the pulse duration and the FT limit at the end of the crystal for all four cases.

the same results. This confirms our assumption that for pulses longer than 100 fs dispersion is negligible.

According to Eq. 3.3 a longer crystal length  $L$  as well as higher input intensity  $I$  increase conversion efficiency. That means if we only consider XPW, spectral broadening is independent of conversion efficiency and can be quantified by multiplying the input spectral width by  $\sqrt{3}$  in agreement with theory. If we include XPW and SPM or XPW and XPM, we see inhomogeneous and less spectral broadening than if we include XPW, SPM and XPM. Therefore we can conclude that the additional spectral broadening we found in experiment for higher conversion efficiency is not caused by a single nonlinearity independently from the others but by an interplay of XPM between the XPW and the incident pulse and SPM of the XPW pulse.

Fig. 3.10 shows the evolution of the pulse duration and the FT limit while propagating along the crystal. At the beginning the pulse duration agrees with the theory value of 565 fs and the pulse is FT limited for all cases. Case A, where all effects are included, represents the experiment. The pulse duration stays close to the theory value all throughout the crystal and the FT limit decreases to 300 fs. In Case B the pulse duration and the FT limit are almost constant and the pulse stays FT limited while propagating. The slight increase of the pulse duration cannot be caused by dispersion because simulating without dispersion results in the same values.

In Case C and D the pulse duration increases and reaches almost the input pulse duration in Case D. As can be seen from Fig. 3.10 -b the deviation of the pulse duration from the FT limit at the end of the crystal is 350 fs in Case C and 500 fs in Case D.

To understand the behavior of the pulse duration and the FT limit we have to look at the GDD of the XPW pulse. Fig. 3.11 shows the GDD for Case A to D at the end of the crystal and the according spectra as well as the spectrum of the input pulse. For Case B the GDD is zero which means that the pulse is unchirped and preserves its FT limited. For Case A the GDD

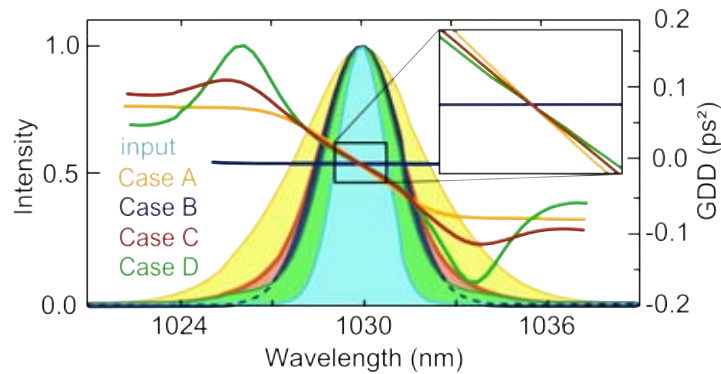


**Figure 3.11:** Simulated Group delay dispersion (GDD) of the XPW pulse after propagating through a 6 mm  $(BaF)_2$  crystal for Case A to D. As a reference the corresponding output XPW spectra are shown.

has a linear slope resulting in a nearly constant pulse duration and a decreasing FT limit. For Case C and D the GDD increases steeper than linearly at the edge of the pulse spectrum. This might cause pulse elongation and the large deviation from the FT limit. The shown spectra emphasize once more that the spectrum broadens less and inhomogenous if we include XPW and either SPM or XPM. For XPW and XPM the resulting spectrum is not Gaussian and has a broad pedestal.

In conclusion our simulation results show that the XPW process itself does not induce any spectral phase. That means for a FT limited input pulse the XPW pulse is also FT limited but spectrally broadened and self-compressed by  $\sqrt{3}$ . At higher conversion efficiency SPM and XPM start contributing. As a result of the interplay of both effects we see additional spectral broadening that exceeds the theory broadening factor of  $\sqrt{3}$ . At the same time the pulse acquires chirp and the pulse duration deviates from the FT limit.

### 3.3.2 Influence of the spectral phase

As we now know that operating the first XPW stage at a conversion efficiency above 5 % introduces spectral chirp, it is self-evident to assume that the introduced chirp influences the second XPW stage.

#### Simulation

To prove this assumption we first simulated the XPW process based on the measurement of the first XPW stage as input pulse. The retrieved data of the FROG measurement allows us to simulate two distinct cases. Calculating the input pulse by Fourier transforming the retrieved spectrum with spectral phase zero results in a FT limited pulse. Calculating the input pulse by Fourier transforming the retrieved spectrum with the retrieved spectral phase yields a pulse with the same spectral phase and time envelope than in experiment. The peak intensity was

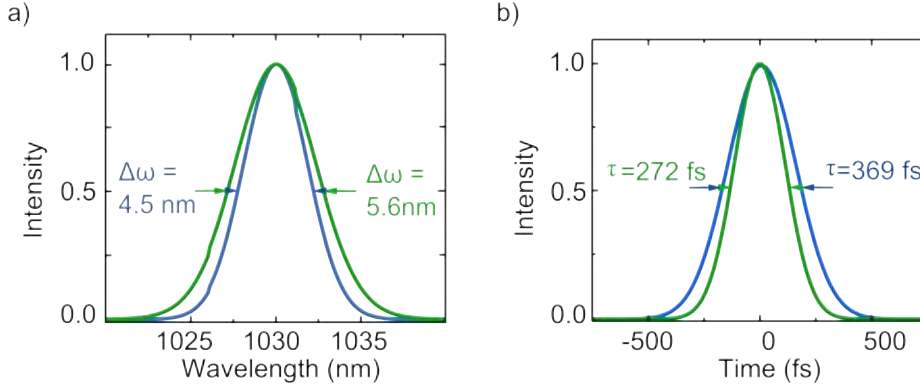


**Figure 3.12:** Simulated spectra and time envelopes for a FT limited input pulse (blue line) and a chirped input pulse (green line).

chosen to achieve the same conversion efficiency as in experiment. The input pulse duration is 537 fs for the chirped pulse and 430 fs for the FT limited pulse. The input spectral width is 3.0 nm.

Fig. 3.12 shows the results of the simulation in time and frequency domain. If the input pulse is chirped, the XPW pulse has a pulse duration of 369 fs and a spectral width of 4.5 nm. These values are in good agreement with the measured FROG traces of the second XPW stage without compression. The calculated broadening and shortening factor is 1.5. If the input pulse is FT limited, the XPW pulse has a pulse duration of 272 fs and a spectral width of 5.6 nm. In this case  $F_{\Delta\lambda} = 1.8$  and  $F_{\Delta\lambda} = 1.6$ . The simulation shows that the spectral phase has an influence on the XPW process. For FT limited input pulses we see more spectral broadening and shorter XPW pulses.  $F_{\Delta\lambda}$  and  $F_{\Delta\lambda}$  are closer to the theory value of  $\sqrt{3}$ .

To analyze the influence of the spectral phase on the pulse shortening and spectral broadening in XPW we did a series of simulations. The basis for the simulation were various FROG measurements of the first XPW stage. The measurements were conducted at different conversion efficiency. As discussed in the previous section with increasing conversion efficiency we see additional spectral broadening that causes the XPW pulse to acquire a higher GDD. The maximum GDD of each measurement was calculated taking the second derivative of the retrieved spectral phase with respect to angular frequency. Since the input spectral width for different measurements changes the spectral width of the output XPW pulse is not directly comparable. Therefore we compared the spectral broadening factor  $F_{\Delta\lambda}$  for different GDD values. Fig. 3.13 shows a comparison between the broadening factors for FT limited pulses (blue dots) and for chirped pulses (green squares). The linear fit of the blue dots shows that the broadening factor for the FT limited pulses is nearly constant for all measurements. The negative slope of the linear fit of the green squares indicates that the broadening factor decreases for input pulses based on measurements with increasing GDD. For a GDD higher than  $0.08(\text{ps})^2$  the broadening factor is below the theory value. That means we see less broadening than predicted by theory. For a GDD between  $0.08(\text{ps})^2$  and  $0.02(\text{ps})^2$  the broadening factor is above the theory value but below the value that can be reached for FT limited input pulses. For a GDD smaller than  $0.02(\text{ps})^2$  the broadening factor for chirped input pulses approaches

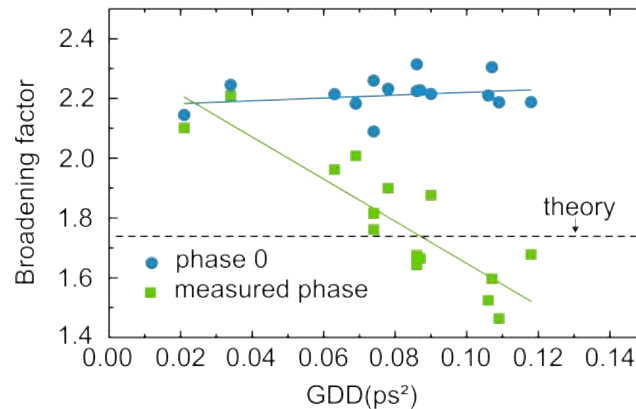


**Figure 3.13:** Simulated broadening factor for input pulses with increasing GDD (green squares). As a comparison the broadening factor for the same pulses with spectral phase zero is shown (blue dots). The solid lines denote a linear fit of the according data points. The dashed line shows the theory broadening factor  $\sqrt{3}$ .

the constant value for FT limited pulses. The deviation from theory can be explained by additional spectral broadening as discussed previously.

These results show that the spectral broadening occurring during the XPW process is correlated to the chirp of the input pulse. For increasing GDD we see a decreasing spectral width of the XPW pulse.

### Pulse compression

The next step is to prove this hypothesis experimentally by operating the compression stage from Fig. 3.5 -c. To estimate the chirp acquired in the first XPW stage the GDD was calculated by taking the second derivative of the spectral phase retrieved from the FROG measurement of XPW 1 with respect to the angular frequency. The GDD reaches values of  $0.058 \text{ ps}^2$ . From Fig. 3.6 the according grating distance to compensate for this amount of GDD can be identified. At an incident angle of  $\theta = 30^\circ$  the grating distance must be about 25 mm to achieve a GDD of  $-0.058 \text{ ps}^2$ . We placed the gratings according to these considerations and characterized the compressed pulse with the FROG. The grating distance was further optimized to achieve the flattest spectral phase and the smallest deviation between pulse duration and FT limit. Fig. 3.14 shows the results for optimized grating distance in time and frequency domain. The spectra for the compressed (solid green line) and the uncompressed (solid blue line) pulse have the same spectral width and the same shape but the spectral phase of the compressed (dashed green line) pulse is flat whereas the spectral phase (dashed blue line) of the uncompressed pulse is curved. In time domain the flat spectral phase translates to a FT limited pulse (solid green line). The pulse is compressed from 537 fs to 404 fs. The good agreement of the FT limit of the uncompressed pulse (red line) with a full width half maximum of 398 fs and the compressed pulse shows that the compression stage serves its purpose.

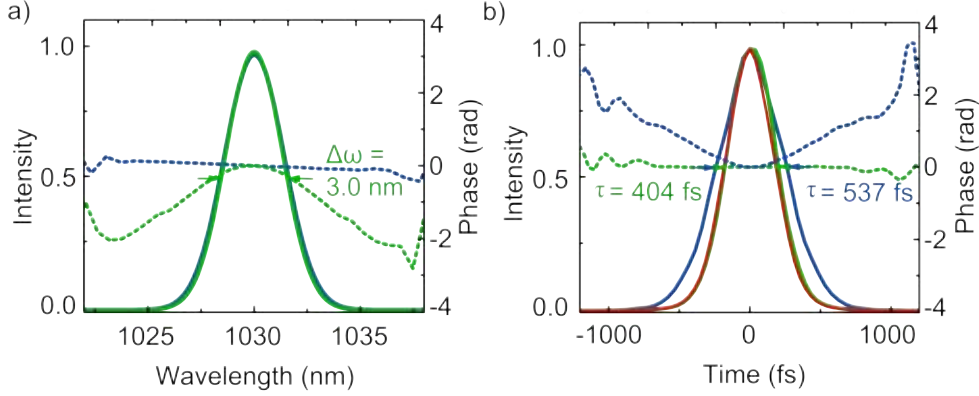


**Figure 3.14:** Pulse compression: Retrieved spectrum (a) and retrieved time envelope (b) of the XPW pulse after the first stage without (solid blue line) and with compression (solid green line). The dashed lines show the spectral phase and the phase, respectively. The solid red line denotes the FT limit of the uncompressed pulse.

## Experiment

By employing the compression stage, we gained the possibility to experimentally observe the influence of the spectral phase on the XPW process. We repeated the FROG measurement of the XPW pulse after the second stage with FT limited input pulses at a conversion efficiency of 3 %. In Fig. 3.15 a comparison between the results for an uncompressed (solid blue line) and a compressed input pulse (green line) is shown. The XPW pulse for a compressed input pulse has a spectral width of 5.2 nm and a pulse duration of 244 fs. In agreement with the simulation we see more spectral broadening and shorter pulses if the input pulse is FT limited. For chirped input pulses we calculated  $F_\tau$  is 1.6 and  $F_{\Delta\lambda}$  is 1.5. For unchirped input pulses  $F_\tau$  and  $F_{\Delta\lambda}$  are both 1.7 which agrees with the theory value of  $\sqrt{3}$ . Another difference between the two measurements is that for compressed input pulses the XPW pulse is FT limited. The red line in Fig. 3.15 denotes the FT limit of the XPW pulse for compressed input pulses with a full width half maximum of 240 fs. Another indicator is the flat spectral phase (Fig. 3.15-b, dashed green line) in the case of compressed input pulses. The FT limit of the XPW pulse for chirped input pulses is not shown graphically for clarity reasons but has a full width half maximum of 280 fs.

These experimental results confirm our hypothesis based on the simulation results. The spectral phase of the input pulse has an influence on the spectral broadening and pulse shortening occurring during the XPW process. The downward deviation from the theory value for  $F_\tau$  and  $F_{\Delta\lambda}$  is caused by the chirp of the input pulse. If the XPW pulse is generated by an unchirped pulse,  $F_\tau$  and  $F_{\Delta\lambda}$  agree with the theory value. In the second XPW stage the conversion efficiency is in a regime where no other nonlinearities like SPM and XPM contribute. Therefore we see no upward deviation from theory. This is also the reason why the XPW pulses for compressed input pulses are FT limited. If only XPW contributes, no spectral phase is induced on the XPW pulse and it preserves its FT limit. If the input pulse is already chirped, the

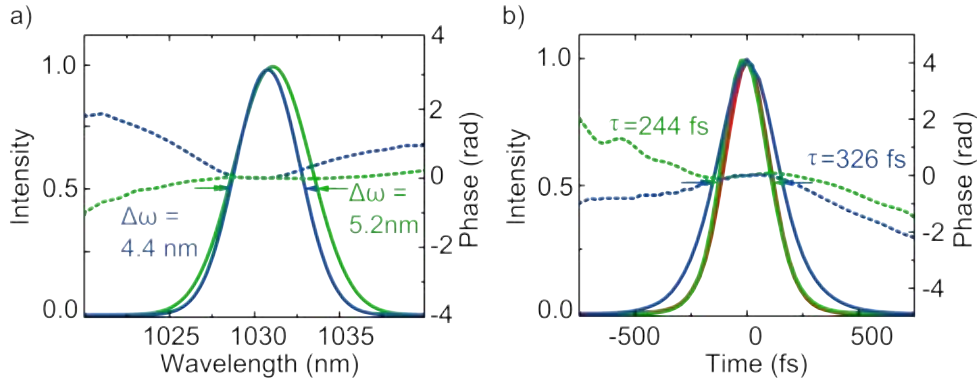


**Figure 3.15:** Influence of the spectral phase: Retrieved spectra (a) and retrieved time envelopes (b) of the XPW pulse after the second stage for an uncompressed (solid blue line) and a compressed input pulse (solid green line). The dashed lines show the spectral phase and the phase, respectively. The solid red line denotes the FT limit of the compressed pulse.

XPW pulse is chirped as well.

Removing the chirp of the XPW pulse after the first stage by employing the transmission gratings allows us to compress the 1-ps input pulses to less than 250 fs. At the same time the spectrum is broadened from 1.6 nm to 5.2 nm.

### 3.4 Summary and conclusion

At the beginning of this chapter the principles of cross-polarized wave generation were explained. It is a degenerate four wave mixing process that occurs in crystals with a  $\chi^{(3)}$  anisotropy. An intense, linearly polarized input pulse generates a pulse with orthogonal polarization with respect to the input pulse. The generated XPW pulse is spectrally broadened and shortened by  $\sqrt{3}$ . The crystal of choice is BaF<sub>2</sub> with holographic cut because of its high  $\chi^{(3)}$  anisotropy and its broad transmission bandwidth ranging from the UV to the NIR. To experimentally optimize the conversion efficiency of the XPW process, the crystal length, the beam divergence, and the peak intensity on the crystal surface have to be chosen carefully to find a trade-off between damage threshold, self-focusing and spatial walk-off of the incident and the generated pulse.

We managed to run a cascaded XPW setup which allows spectral broadening and pulse shortening by more than a factor of 3. With a grating compressor between the first and the second XPW stage the 1-ps input pulses were shortened down to 244 fs. The conversion efficiency was 9 % in the first stage and 3 % in the second stage which yields a total conversion efficiency of 0.3 %.

In experiment we observed that for conversion efficiency higher than 5 %, the spectral width of the XPW pulse exceeds the theory value calculated by multiplying the input spectral width by  $\sqrt{3}$ . By simulating the XPW process for different third-order nonlinearities, we found that this additional spectral broadening is caused by an interplay of SPM and XPM. At lower

conversion efficiency only XPW contributes and we do not see additional spectral broadening. In this case the spectral phase of the generated pulse is not affected.

With our numerical and experimental results we could prove that the spectral phase influences the XPW process. For chirped input pulses we saw less spectral broadening and less pulse shortening than predicted by theory. When we compressed the pulses before sending them to the XPW stage the spectral width and the pulse duration agreed with theory.

Besides these interesting findings, that help to understand the fundamental principles of the XPW process, the practical application of cascaded XPW is doubtful. The limitation of the total conversion efficiency to less than 1 % due to the damage threshold of BaF<sub>2</sub> raises the question if pulse shortening by  $\sqrt{3}$  in a second stage justifies the decrease of total conversion efficiency by more than one order of magnitude.

An alternative approach is to employ a single XPW stage and send the shortened output pulses to a bulk crystal for continuum generation. Such a setup takes advantage of temporal pulse cleaning, spectral smoothening, and beam profile enhancement happening during XPW. At the same time the  $\sqrt{3}$  pulse shortening helps to avoid the drawbacks of continuum generation from 1 ps pulses.

# Chapter 4

## Cascaded second-order nonlinearities

Operating second-order nonlinearities out of phase matching results in an effective third-order nonlinearity. By changing the phase matching angle, one can build a device with a Kerr-like nonlinearity tunable in magnitude and sign [69]. This all-optical induced nonlinear refractive index can be utilized for the self-compression of positively chirped pulses [70] as well as for Kerr lens mode locking [71, 72]. However, the approach presented in this chapter employs the induced self-focusing for spectral broadening via SPM. The spectrally broadened pulses are compressed using transmission gratings. In a two-step setup we realized the compression of 1 ps pulses down to less than 150 fs with a conversion efficiency close to 50 %.

The following chapter gives an insight into the processes happening in cascaded second-order nonlinearities, explains the used setup and discusses the experimental results.

### 4.1 Phase modulation in second-order nonlinear processes

In third-order nonlinear processes like SPM and XPM the intensity dependence of the refractive index of a nonlinear medium introduces a phase modulation on a pulse propagating in this medium. Due to the temporal variation of the intensity, the phase velocity varies and the pulse acquires a phase modulation. This phase modulation leads to the generation of new frequencies and the pulse is spectrally broadened.

In comparison to third-order nonlinearities, second-order nonlinearities can only produce phase modulation if the interaction takes place with a certain amount of phase mismatch [73]. Phase mismatched second-order processes offer the advantage of efficient phase modulation at low input intensity and short interaction length because the  $\chi^{(2)}$  of nonlinear crystals is in general much higher than the nonlinear refractive index.

In the case of cascaded second harmonic generation (SHG) the fundamental (FW,  $\omega_1$ ) and the generated second harmonic (SH,  $\omega_2 = 2\omega_1$ ) are not phase-matched, i.e. the wave vector mismatch  $\Delta k = k_{2\omega} - 2k_\omega$  between both beams does not vanish. The SHG process can be described by the following coupled wave equations derived from Maxwell's equations using

the slowly evolving envelope approximation:

$$\begin{aligned}\frac{dE_1}{d\zeta} &= -i \frac{\omega}{4cn_\omega} \chi^{(2)}(\omega; 2\omega, -\omega) E_2^* E_1 \exp(-i\Delta k\zeta), \\ \frac{dE_2}{d\zeta} &= -i \frac{\omega}{2cn_{2\omega}} \chi^{(2)}(2\omega; \omega, \omega) E_1^2 \exp(i\Delta k\zeta).\end{aligned}\quad (4.1)$$

Here  $E_1$  is the complex amplitude of the FW,  $E_2$  the complex amplitude of the SH,  $\zeta$  the propagation direction,  $c$  the speed of light,  $\omega$  the fundamental frequency,  $n_\omega$  the refractive index of the FW,  $n_{2\omega}$  the refractive index of the SH, and  $\chi^{(2)}$  the second-order susceptibility tensor. Equation 4.1 implies that up-conversion to the SH starts decreasing after a coherence length of  $\pi/|\Delta k|$  and is followed by the inverse process of back-conversion to the FW after another coherence length [74]. Upon further propagation both processes cyclically repeat themselves. Figure 4.1-a shows the depletion of the fundamental (intensity of the fundamental over the input intensity) as a function of the phase mismatch after a certain propagation length  $L$  (crystal length). In the case of phase matching, the fundamental sees the largest depletion. Out of phase matching, the intensity of the fundamental increases upto the minimum of the SH and starts decreasing. During the process of back-conversion the fundamental experiences a

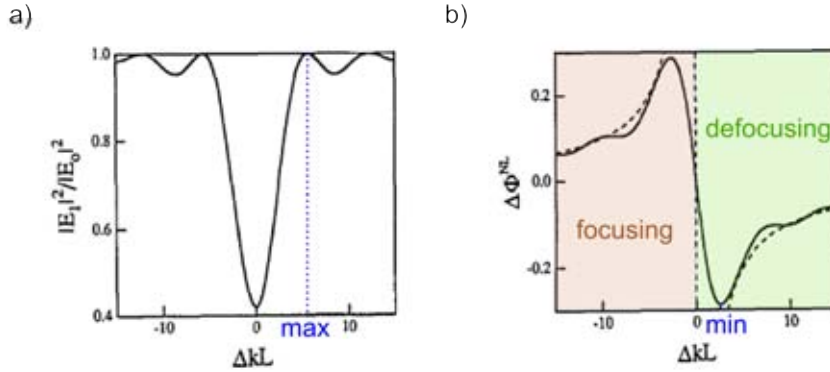


**Figure 4.1:** Calculated intensity of the fundamental over the input intensity (a) and calculated nonlinear phase shift of the fundamental (b) as a function of the phase matching angle and the crystal length in cascaded SHG. Adapted from: "Self-focusing and self-defocusing by cascaded second-order effects in KTPR.", by R. De Salvo et al., 1992, Opt. Lett., 17, 1, p. 29.

nonlinear phase shift  $\Delta\Phi^{NL}$  which can be calculated from Eq. 4.1 assuming that depletion of the fundamental can be neglected [69]:

$$\Delta\Phi^{NL} \approx \frac{\Delta kL}{2} (1 - \sqrt{1 + (2\Gamma/\Delta k)^2}). \quad (4.2)$$

Here  $L$  is the crystal length and the parameter  $\Gamma$  is defined as

$$\Gamma = \frac{\omega d_{\text{eff}} |E_0|}{c \sqrt{n_\omega n_{2\omega}}}, \quad (4.3)$$

where  $d_{\text{eff}}$  depends on the second-order susceptibility  $\chi^{(2)}$  of the nonlinear crystal and  $E_0$  is the amplitude of the incident wave. In Fig. 4.1-b the nonlinear phase change  $\Delta\Phi^{NL}$  is depicted as a function of the phase mismatch  $\Delta k$  and the crystal length  $L$ . In the case of large phase mismatch Eq. 4.2 simplifies to (dashed line in Fig. 4.1-b):

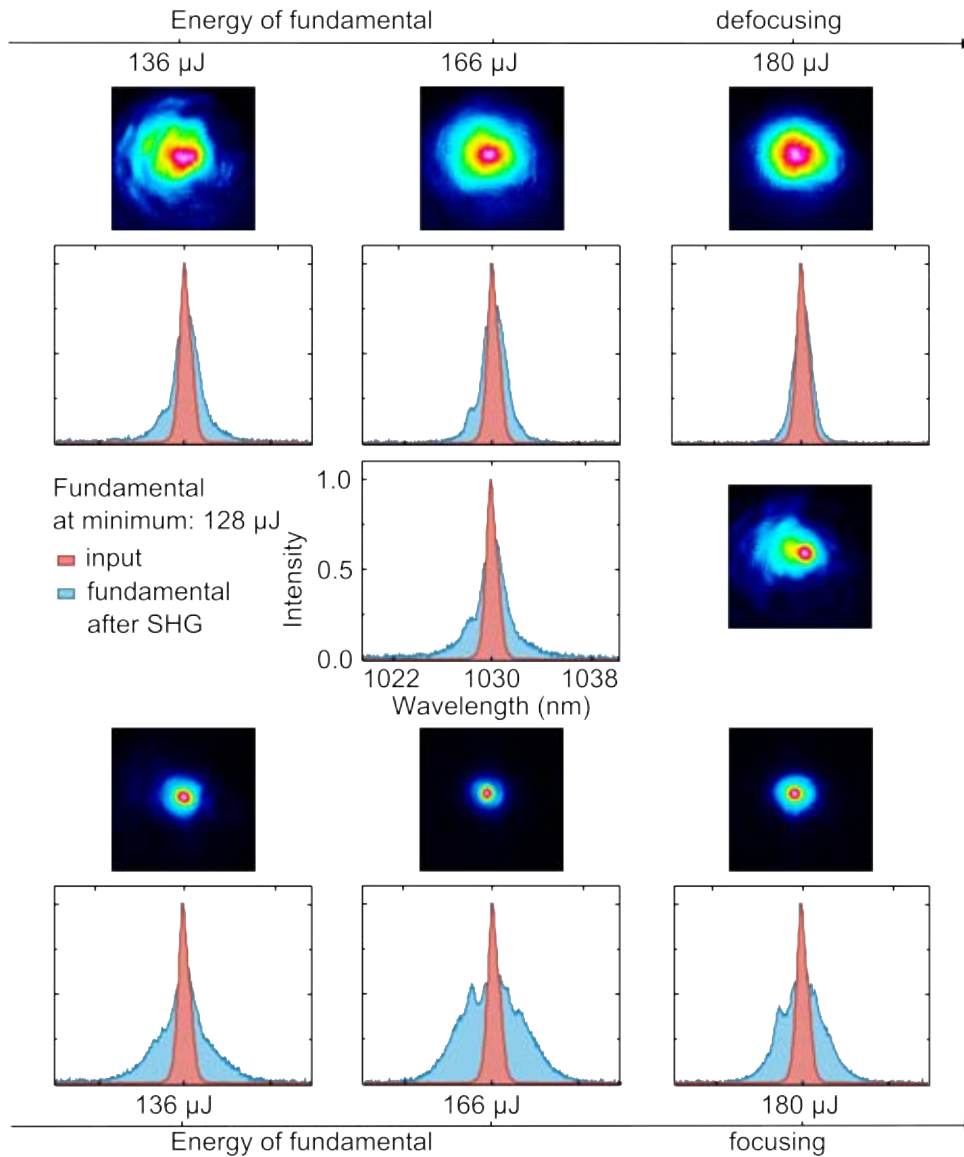
$$\Delta\Phi^{NL} \approx -\frac{\Gamma^2 L^2}{\Delta k L}. \quad (4.4)$$

This implies a linear dependence of the phase shift on the incident intensity which is similar to the optical Kerr effect where  $n = n_0 + n_2 I$ . According to the Kerr effect we can define an effective nonlinear refractive index  $n_2^{\text{eff}}$ :

$$n_2^{\text{eff}} = \frac{-4\pi L}{c\epsilon_0} \frac{d_{\text{eff}}^2}{\lambda n_\omega^2 n_{2\omega}} \frac{1}{\Delta k L}, \quad (4.5)$$

where  $\lambda$  is the incident wavelength and  $\epsilon_0$  the electric permittivity. Changing the phase matching angle allows us to tune the effective nonlinear refractive index in magnitude and sign. For  $\Delta k < 0$  we end up in the self-focusing regime and for  $\Delta k > 0$  in the self-defocusing regime [74]. However, there is an asymmetry between both regimes, because before self-defocusing takes place, the positive nonlinear refractive index due to the electronic Kerr effect has to be compensated. Figure 4.1-b does not show this asymmetry because the electronic Kerr effect was not taken into account.

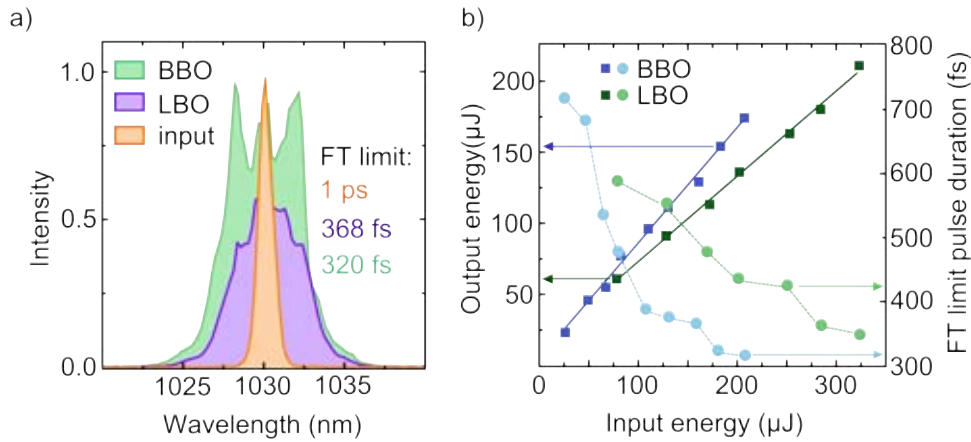
To illustrate the induced changes on the fundamental, we recorded the spectra and the beam profiles of the fundamental for different phase matching angles after SHG in a 3 mm thick type I BBO crystal. Figure 4.2 shows the results of this study. First the BBO crystal was rotated until the SH energy reached its maximum at 68  $\mu\text{J}$ . In this position the phase matching condition is fulfilled. The according spectrum and beam profile are depicted in the center of Fig. 4.2. The red line shows the spectrum of the incident wave for comparison. If we change the phase matching angle of the crystal away from  $\Delta k = 0$ , the energy of the fundamental increases and the energy of the SH decreases in agreement with Fig. 4.1-a. In one direction  $\Delta k$  becomes positive and we end up in the defocusing regime (Fig. 4.2, upper row), in the opposite direction  $\Delta k$  becomes negative and we end up in the focusing regime (Fig. 4.2, lower row). The FW energy is steadily increasing and we cannot enter the second up-conversion cycle of the SH because the tilting angle of the crystal is limited by the small aperture. Experimentally the focusing regime can be recognized by the decreasing beam diameter and the broader spectrum in comparison to the incident wave. Self-focusing causes SPM and new frequencies are generated. The smallest beam diameter and the broadest spectrum does not coincide with the highest FW energy. This behavior is in agreement with Fig. 4.1, where the nonlinear phase shift reaches its minimum before the FW energy reaches its first maximum. In the defocusing regime the situation is different. The spectrum gets narrower and the size of the center of the beam increases until the FW energy reaches 180  $\mu\text{J}$ . At this point the spectrum is equal to the incident spectrum. If we go beyond this point, the beam diameter will increase and the spectrum will broaden again because the nonlinear phase shift is still increasing. As discussed previously, this asymmetry between the focusing and the defocusing regime is caused by the electronic Kerr effect.



**Figure 4.2:** Spectra and beam profiles of the fundamental wave after SHG in a 3 mm thick BBO crystal for different fundamental energies. By increasing the phase mismatch the fundamental sees less depletion. The red spectrum shows the spectrum of the incident wave for comparison.

## Maximizing spectral width and conversion efficiency

As we want to operate cascaded SHG for the pulse compression of 1 ps pulses, we need to maximize the spectral broadening and the transmittance of the fundamental. From Eq. 4.4 it can be seen that the nonlinear phase shift is proportional to  $d_{\text{eff}}^2$ , the input intensity  $|E_0|^2$ , and the crystal length  $L$  and inversely proportional to the phase mismatch  $\Delta k$ . In the experiment the phase matching angle is always adjusted to achieve the broadest spectrum of the fundamental. Due to the asymmetry between focusing and defocusing the system is always operated in the self-focusing regime. Since  $d_{\text{eff}}$  depends on the second-order susceptibility of the crystal we compared two different types of crystals: a BBO, type I crystal with a thickness of 4 mm and a LBO, type I crystal with the same thickness.



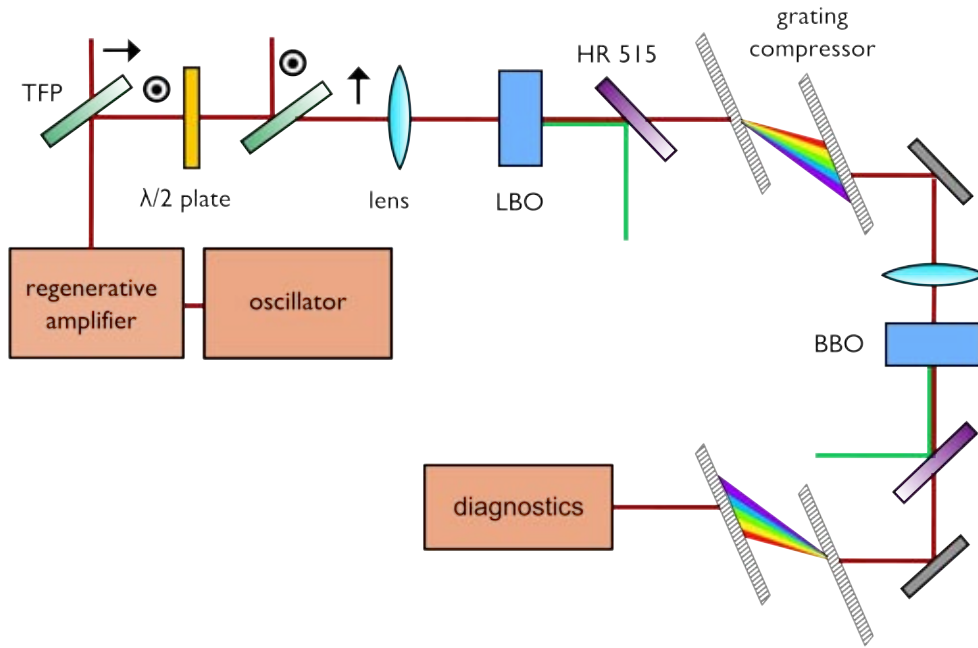
**Figure 4.3:** Comparison between BBO and LBO: a) Spectra of the incident wave (orange) and the FW after SHG in BBO (green) and in LBO (purple). b) Energy (squares) and FT limit pulse duration (dots) of the fundamental after SHG in BBO (green) and in LBO (blue) as a function of the input energy. The solid lines show a linear fit of the FW energy which corresponds to the conversion efficiency. The dashed lines are a guideline for the eye.

Figure 4.3-a shows the broadest spectra that could be achieved in BBO and in LBO. The FT limit pulse duration was calculated to 320 fs in the case of BBO and 368 fs in the case of LBO. The nonlinear phase shift scales linearly with the input intensity. Therefore we scanned the input energy for both crystals and recorded the according spectra and FW energy. From the spectra the FT limit pulse duration can be calculated. The results of the energy scan are shown in Fig. 4.3-b. A linear fit (solid line) of the FW energy reveals the conversion efficiency. The conversion efficiency amounts to 81 % for BBO and 61 % for LBO. The FT limit pulse duration decreases with increasing input energy. The shorter FT limit pulse duration at lower input energy and the higher conversion efficiency make BBO the more preferable candidate in comparison to LBO.

By finding a good trade-off between crystal length and phase mismatch, the conversion efficiency could be further optimized. But due to the lack of suitable crystals and the difficult realization of scaling the crystal length with less than 0.5 mm difference this parameter was not further optimized.

## 4.2 Experimental setup for pulse compression with cascaded SHG

After these preliminary experiments we designed a setup consisting of two consecutive, phase mismatched SHG crystals. Each crystal is followed by a transmission grating pair to recompress the fundamental in time. Figure 4.4 shows a sketch of the setup.



**Figure 4.4:** Cascaded SHG setup: The p-polarized, 1 ps pulses are focused to a phase mismatched LBO crystal. The FW is separated from the SH and temporally compressed with transmission gratings. Consecutively, the process is repeated in a phase mismatched BBO crystal.

Up to the first lens the setup is identical to the setup used for cascaded XPW. The attenuator consisting of a TFP and a  $\lambda/2$ -plate is retained to be able to scale the input energy. Hence, the input pulses are p-polarized. A convex lens with  $f=500$  mm is used to focus the beam to the first SHG crystal. The 4 mm thick, type I LBO crystal with  $\theta = 24^\circ$  is placed approximately 30 mm behind the focus of the lens. Although we found that the spectral broadening and the conversion efficiency in BBO crystals is higher we had to use a LBO crystal due to the lack of suitable BBO crystals. Rotation angle and horizontal tilting angle of the crystal are adjusted to maximize the SH signal. The vertical crystal angle is tilted away from the phase matching angle and fixed at the position of the broadest fundamental spectrum. After the crystal the SH and the FW are separated with a harmonic separator that reflects at 515 nm. The spectrally broadened fundamental is temporally compressed using a pair of transmission gratings (Light Smith, LSGF-1000) with a groove density of  $1000 \text{ mm}^{-1}$  in single-pass configuration. At an incident angle of  $30^\circ$  and a grating distance of 35 mm the introduced GDD is  $-0.082 \text{ ps}^2$  (see Fig. 3.6).

Using a convex lens with  $f=175$  mm, the compressed pulses are focused to a second SHG crystal. The 4 mm thick, type I BBO crystal with  $\theta = 24^\circ$  is placed about 20 mm behind the focus of the lens. The alignment procedure for the crystal is identical to first SHG crystal. Another harmonic separator is employed to reflect the SH and transmit the FW. The FW is sent to a second transmission grating pair of the same type. At an incident angle of  $30^\circ$  and a grating distance of 5 mm the second grating pair introduces a GDD of  $-0.011$  ps<sup>2</sup>. Both the compressed pulses after the first grating and after the second grating can be sent to a SHG-FROG (same characteristics as for cascaded XPW) for characterization.

### Conversion efficiency of the system

To characterize the setup the transmission of each element was measured for varying input energy. The results are shown in Fig. 4.5.

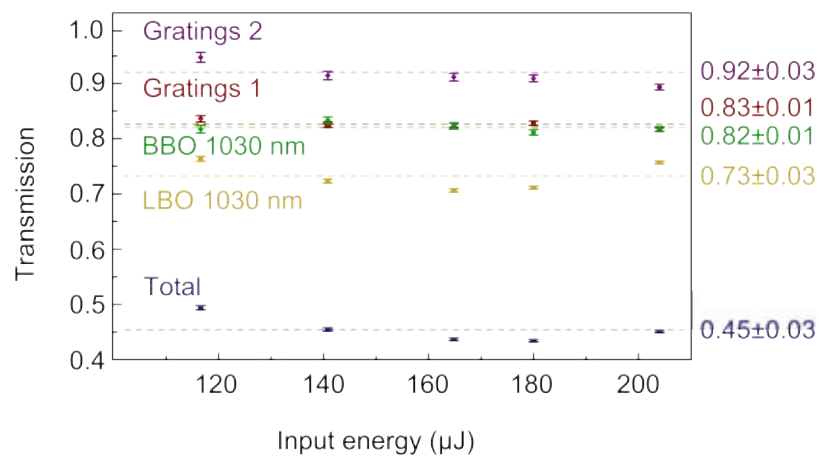


**Figure 4.5:** Transmission of the different optical components as a function of the input energy. The dashed lines show the average values. The total transmission was measured at the output and agrees with the product of the single transmission values.

In agreement with Fig. 4.3-b, the conversion efficiency of the spectrally broadened fundamental in BBO is 82 %. The conversion efficiency of the fundamental in LBO is 73 %, which is higher than the 61 % from Fig. 4.3-b. The difference is caused by a change in the phase matching angle to optimize the conversion efficiency at the cost of a narrower spectrum. However, the change in spectral width is negligible in comparison to the gain in fundamental energy. The transmittance of 83 % of the first grating is too low for single pass configuration. The low value is caused by scratches and damaged spots on the gratings. The transmittance of 92 % of the second grating is more appropriate for single pass configuration. The total conversion efficiency of 45 % was measured at the output of the second grating and agrees with the product of the transmittance of the single elements. This corresponds to an output energy of 92  $\mu$ J for an input energy of 205  $\mu$ J.

The total conversion efficiency of 45 % is a promising value and can be further increased in a final setup by using two BBO crystals instead of one LBO and one BBO crystal, by replacing the damaged grating and by optimizing the crystal thickness. Assuming that the conversion efficiency of the fundamental in BBO can be optimized to 85 % by changing the crystal length, an exchange of the LBO crystal and the damaged grating could increase the total conversion efficiency to 60 %.

The generated second harmonic achieves a maximal energy of 31  $\mu\text{J}$  in the case of LBO and 15  $\mu\text{J}$  in the case of BBO, which corresponds to a conversion efficiency of 15 % and 12 %, respectively. Looking at the transmission of the fundamental, this means that the losses are 12 % in the case of LBO and 6 % in the case of BBO. Sources for losses are reflection and absorption in the crystals as well as transmission of the second harmonic in the harmonic separator. Reasons for the difference in losses can be different anti-reflection coatings, the crystal type, and the different harmonic separators used.

As phase mismatched SHG is an unsaturated process, the generated SH pulse is intrinsically shorter than the input pulse by a factor of  $\sqrt{2}$ . This implies the reuse of the shortened 30  $\mu\text{J}$  pulses from LBO for filamentation in bulk or fiber.

### 4.3 Experimental results

Besides the promising conversion efficiency, the described setup is capable of pulse compression by more than a factor of 6.

The input pulse as well as the output pulses after each grating compressor were characterized using SHG-FROG as described in the previous chapter. The according spectra were recorded with an Ocean Optics HR 4000 spectrometer. Figure 4.6-a, -c, and -e shows the measured and reconstructed FROG spectrograms for the input pulse and the pulses after each grating compressor, respectively. Figure 4.6-b, -d, and -f show the retrieved time envelope and the measured spectra of the input pulses and the pulse after each grating compressor, respectively.

From the spectrograms it can be seen that the pulse gets spectrally broadened after each crystal and temporally compressed after each grating pair. The  $G_{error}$  lies below  $7 \times 10^{-3}$  for all measurements. The input spectrum with a FWHM of 1.6 nm broadens to 4.5 nm after SPM in the phase mismatched LBO crystal. After compression the pulse has a FWHM pulse duration of 397 fs. These values correspond to a broadening factor of 2.8 and a shortening factor of 2.5.

The spectrum after the phase mismatched BBO crystal shows a peak at 1030 nm and its wings range from 1005 nm to 1050 nm. Therefore it is hard to compare the spectra in terms of FWHM. Although the spectrum is not homogeneous, pulse compression works well without any filtering. The compressed pulse has a Gaussian shape and a FWHM pulse duration of 153 fs. This corresponds to pulse shortening by a factor of 2.6 in the second SHG crystal and is comparable to the first SHG crystal. In total the 1 ps input pulses are shortened by a factor of 6.5 in two steps. The measurements were conducted at an input energy of 180  $\mu\text{J}$  and yielded 150 fs output pulses with 80  $\mu\text{J}$  of energy.

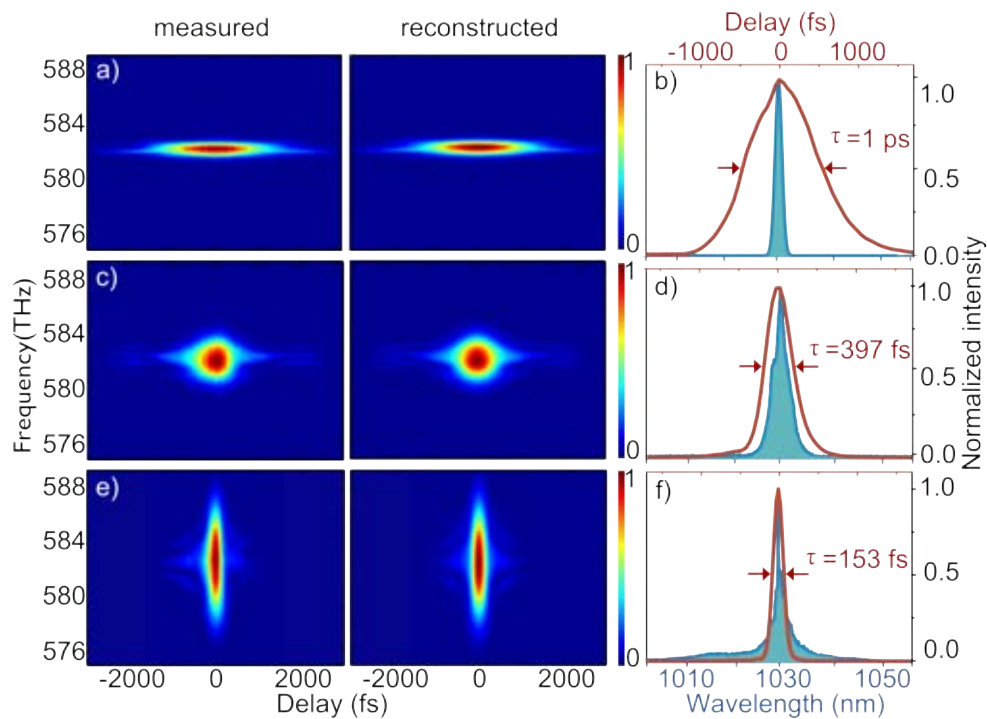


**Figure 4.6:** Characterization of the input pulse and the compressed pulses after each phase mismatched SHG crystal: a), c), and e) show the measured and reconstructed FROG spectrograms of the input pulse and the pulses after each grating.  $G_{error}: 2.8 \times 10^{-3}$ ,  $G_{error}: 4.5 \times 10^{-3}$  and  $G_{error}: 6.4 \times 10^{-3}$ , respectively. b), d), and f) show the retrieved time envelopes (red) and the measured spectra (blue), respectively.

### 4.3.1 Influence of the input intensity

As discussed previously, the induced nonlinear phase shift in cascaded second-order nonlinearities depends linearly on the input intensity. To analyze the influence of changes in the nonlinear phase shift on the spectral width and the pulse duration in our system, we gradually scaled the input intensity by increasing the input energy. For each input intensity, we recorded the spectrum and the FROG trace of the pulse after the first and the second grating compressor. Figure 4.7 shows the recorded spectra for the LBO crystal (a) and for the BBO crystal (b). The term input energy in both diagrams refers to the input energy on the first SHG crystal. The immediate input energy on the BBO crystal corresponds to 73 % of this input energy.

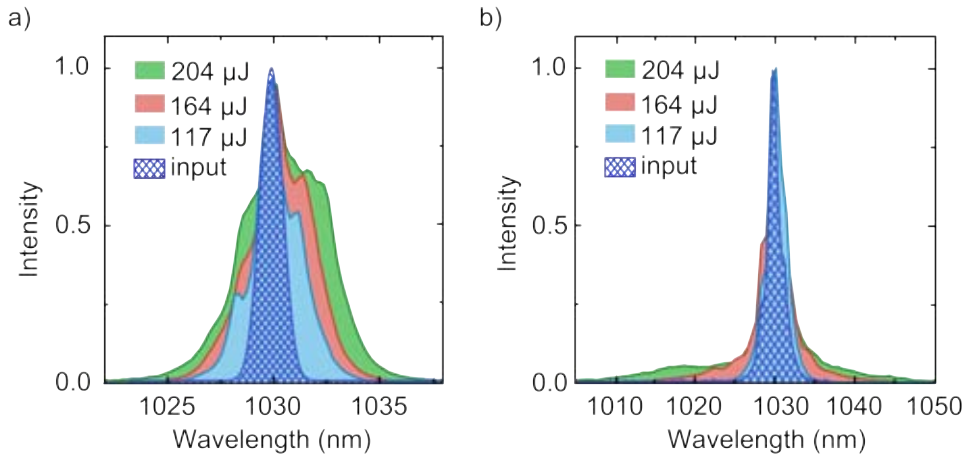


**Figure 4.7:** Spectra after SHG in LBO (a) and in BBO (b) consecutively for different input energies. The plaid parts show the input spectrum, respectively.

For LBO the spectrum broadens almost homogeneously with a small peak at 1030 nm. The FWHM increases from 2.7 nm to 4.5 nm. In the case of BBO, the shown input spectrum (plaid) corresponds to the LBO spectrum at 204  $\mu\text{J}$ . For 117  $\mu\text{J}$  input energy, which corresponds to 89  $\mu\text{J}$  on the BBO crystal, the input spectrum is almost identical to the spectrum after the BBO crystal. At 164  $\mu\text{J}$  input energy the wings of the spectrum extend from 1015 nm to 1045 nm. At 204  $\mu\text{J}$  the wings reach 1005 nm and 1050 nm. For all input energies the center of the spectrum is almost unchanged in comparison to the input spectrum.

To see if the spectral width influences the compression, we analyzed the measured FROG traces. Figure 4.8 shows the retrieved spectral width, pulse duration and FT limit for LBO (a) and BBO (c) for the corresponding input energies. As mentioned before, in the case of LBO the spectral width increases from 2.7 nm to 4.5 nm. The value at 180  $\mu\text{J}$  is higher than the trend. The pulse duration decreases from 465 fs to 390 fs at 180  $\mu\text{J}$ . The smallest value does not coincide with the highest energy but as the other values show a steadily decreasing trend the deviation must be a measurement artifact. The FT limit follows the evolution of the pulse duration with a constant difference of 25 fs. This indicates an imperfect compression and might be caused by higher order dispersion, which cannot be compensated by gratings.

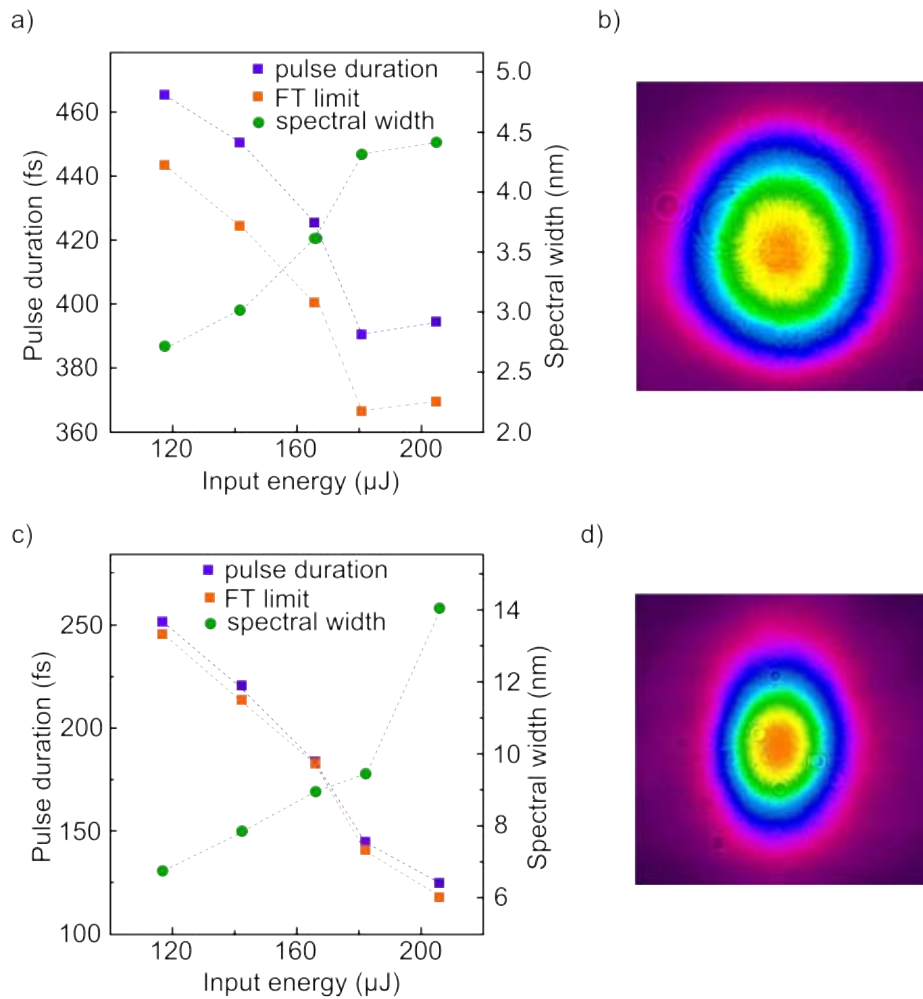


**Figure 4.8:** Spectral width, pulse duration and FT limit retrieved from FROG measurements of the pulse after the first (a) and the second compressor (c) for different input energy. The dashed lines are a guideline for the eye. Beam profile of the fundamental at high energy after LBO (b) and after BBO (d).

In the case of BBO, the spectral width increases from 7 nm to 14 nm and the pulse duration decreases from 250 fs to 125 fs. The difference between the pulse duration and its FT limit is smaller than 5 fs for all energies, which points out the quality of the compression in the second stage.

As the relative change in immediate input energy on the BBO crystal is bigger than the relative change in input energy on the LBO crystal, the relative decrease in pulse duration is 16 % after the first compressor and 50 % after the second compressor for an absolute energy difference of 87  $\mu\text{J}$ . Assuming a linear proportionality between pulse duration and input energy, which is reasonable for the discussed energy range (see Fig.4.8-c, the output pulse duration decreases by 6 % every 10  $\mu\text{J}$  of input energy).

As the induced nonlinear phase shift does not depend on input energy, but on input intensity, this does not limit the energy scalability of the system. However, to keep the output pulse duration constant with varying input energy, the beam diameter has to be rescaled to readjust the input intensity. For high input energies this can require large crystal apertures.

Besides the intensity dependence of the spectral width and the pulse duration, Fig. 4.8-b and -d shows the beam profile of the fundamental after LBO (b) and after BBO (d) for the highest input energy. The beam profile for LBO is almost perfectly round and shows a homogeneous energy distribution along the radial coordinate. The beam profile for BBO is slightly elliptic. The consequences of this degradation in beam quality are discussed in the following subsection.

### 4.3.2 Spatial characterization of the spectrum

To find out how the newly generated frequencies are distributed along the spatial profile of the beam, we recorded spectra of the fundamental after LBO and after BBO for different centrosymmetric fractions of the beam. Therefor we placed a pinhole 80 cm behind the crystals and measured for the fully opened position, the fully closed position and an intermediate position. Figure 4.9 shows the recorded spectra.

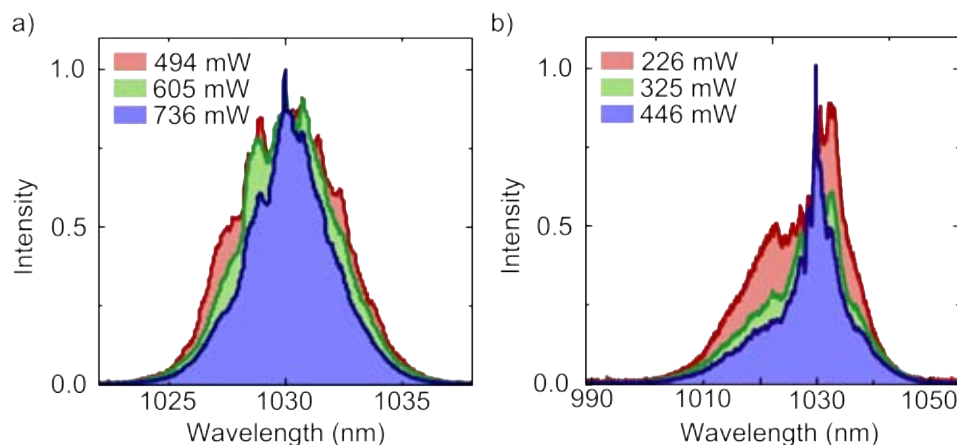


**Figure 4.9:** Spectra of the fundamental after LBO (a) and after BBO (b) for different centrosymmetric fractions of the beam. The fractions were selected using a pinhole.

The beam was not collimated after the crystal and is therefore divergent. For the LBO crystal the change in the spectrum upon closing the pinhole is less pronounced. In the closed position the spectrum is broader and more homogeneous than in the opened position. For BBO the change in the spectral shape is clearly noticeable. When the pinhole is fully opened, the spectrum has a pronounced peak at 1030 nm and broad wings. Upon closing the pinhole, more and more energy is coupled to the wings and the peak gets suppressed. In the fully closed position 67 % of the power is transmitted for LBO and 48 % for BBO. These values are not directly comparable, because the beam divergence in both cases is different. The fact that the spectrum gets broader and the peak at 1030 nm is suppressed if the outer part of the beam is filtered indicates that the new generated frequencies are located in the center of the beam. The outer part contains mainly the original frequencies of the input pulse.

To further use the output pulses of the system, spatial filtering to flatten the spectrum might be considered. In our case it was not necessary, because compression worked well with the unfiltered beam.

## 4.4 Summary and conclusion

At the beginning of this chapter we have seen that phase mismatched second-order nonlinearities effectively act like third-order nonlinearities. In SHG the phase mismatch between the SH and the FW causes back-conversion from the SH to the FW after one coherence length. Upon this back-conversion, the FW experiences a nonlinear phase shift similar to the Kerr effect and gets spectrally broadened. By changing the phase mismatch, the nonlinear phase shift can be tuned in magnitude and sign. This leads to self-focusing and self-defocusing, respectively. Because the second-order susceptibility  $\chi^{(2)}$  of material is in general much larger than its nonlinear refractive index, this approach is particularly suitable for long input pulses, i.e. low intensity.

In the described setup, the SPM on the fundamental after SHG in phase mismatched BBO and LBO crystals is utilized for pulse compression of 1 ps pulses. With two consecutive crystals followed by transmission gratings the pulses could be compressed to less than 150 fs. The proof-of-principle setup used in this thesis already has a conversion efficiency of 45 % and delivers output pulses with upto 92  $\mu$ J.

As a preliminary study to optimize the performance of the setup, we tested different types of crystals. With the use of the right crystal and crystal length, the conversion efficiency can be increased above 60 %.

We also analyzed the influence of the input intensity on the pulse duration as well as the spatial homogeneity of the spectrum. We found that output pulse duration decreases with increasing input intensity and the newly generated frequencies are located in the center of the beam. The outer part of the beam contains mainly frequencies close to the input frequency at 1030 nm.

The approach based on cascaded second-order nonlinearities offers an effective tool for pulse compression of 1 ps pulses. The SH generated as a by-product might also be reused. The energetic 150 fs output pulses are a good starting point for any of the conventional pulse shortening techniques described in Chapter 2.

# Chapter 5

## Spectral broadening using multiple thin plates

Having in place 150 fs energetic pulses, the question for the next step towards an ultra broad-band continuum arises. In Chapter 2 three common spectral broadening techniques were discussed: LMA, HCF, and bulk media. All of these techniques were successfully applied to pulses with few hundred femtoseconds duration [75, 40, 49]. Because of its novelty and simplicity we tested a method based on SPM in multiple thin fused silica plates. It offers the advantage of high input energies and high conversion efficiency because it prevents self-focusing.

The following chapter explains the differences between the used method and common spectral broadening in bulk and presents preliminary experimental results.

### 5.1 Self-phase modulation and self-focusing in thin plates

If the power, a nonlinear medium is exposed to, exceeds a critical value  $P_c$  the beam undergoes self-focusing and collapses [76]. The critical power  $P_c$  is defined by the center wavelength of the beam  $\lambda$ , the linear refractive index  $n_0$ , and the nonlinear refractive index  $n_2$ :

$$P_c = \frac{\pi(0.61)^2 \lambda^2}{8n_0 n_2}. \quad (5.1)$$

Beam collapse leads to beam profile distortion and causes spatial losses [42]. Spatial losses are the main limiting factor for the efficiency of spectral broadening in bulk [77]. The easiest way around this limitation is to keep the length of the bulk medium shorter than the critical self-focusing length  $z_{sf}$  and avoid beam collapse [76]. The critical self-focusing length  $z_{sf}$  is defined as:

$$z_{sf} = \frac{\pi d^2}{\lambda(\sqrt{P_p/P_c} - 1 - \theta)}, \quad (5.2)$$

where  $d$  is the beam diameter at the input surface of the medium,  $P_p$  the peak power of the laser pulse, and  $\theta$  the beam divergence [78]. In this way the input power can exceed the critical power  $P_c$  by many multiples without causing material damage and beam profile distortion. To increase the critical self-focusing length one can increase the beam divergence  $\theta$  and the beam diameter  $d$ . But increasing the beam diameter  $d$  decreases the peak power  $P_p$  and

therefore reduces spectral broadening [42]. This contrary evolution shows that self-focusing and SPM cannot be decoupled [77]. To minimize self-focusing and maximize SPM, Centurion et al. [76] proposed a layered medium consisting of an alternating sequence of glass plates and air gaps. The variation in the nonlinear refractive index from layer to layer leads to an oscillation of the beam width which prevents beam collapse.

Lu et al. [24] realized this idea experimentally for supercontinuum generation in a setup consisting of four 0.1 mm thick fused silica plates. With 25 fs pulses centered at 800 nm they could generate a continuum ranging from 450 nm to 980 nm with 76  $\mu\text{J}$  energy per pulse. This corresponds to a conversion efficiency of 54 % and exceeds all values reported for supercontinuum generation in bulk so far. The reason for this increase in conversion efficiency is the homogenizing effect of the air gaps between the thin plates. Whereas in a single thick plate only the intense center part of the beam is spectrally broadened, in a multiple thin plates setup also the outer parts of the beam become affected. The broadened center diverges faster than the unbroadened outer parts. For the subsequent plates this means that the unbroadened parts move to the most intense region of the beam and also experience spectral broadening [78].

Since supercontinuum generation depends on pulse duration and becomes less efficient and unstable for increased pulse duration [79], the spectral broadening mechanism in our setup is pure SPM. As discussed previously, SPM is a purely temporal nonlinearity and depends on the third-order susceptibility  $\chi^{(3)}$ . Due to the intensity dependence of the refractive index in nonlinear media, the varying intensity along the time-envelope of a pulse introduces a nonlinear phase  $\Phi^{NL}$  [80]:

$$\Phi^{NL}(t) = \omega_0 \frac{\zeta}{c} n_2 I(t). \quad (5.3)$$

Here  $\omega_0$  is the center frequency,  $\zeta$  the propagation direction,  $n_2$  the nonlinear refractive index, and  $I$  the intensity. The nonlinear phase shift modifies the instantaneous frequency of the electric field of the pulse and causes spectral broadening. As can be seen from Eq. 5.3, the nonlinear phase  $\Phi^{NL}$  increases with increasing propagation length  $\zeta$ , but at the same time the interaction length between the pulse and the nonlinear medium must be kept short to avoid self-focusing inside the medium.

These considerations affect the search for the optimum plate thickness. Of course also the beam divergence, the pulse duration, the length of the air gap, and the pulse energy influence the performance of the multiple thin plate setup. Although the principle is rather simple, the variety of tunable parameters makes the experimental realization and optimization challenging.

## 5.2 Experimental setup

A set of different plate thicknesses and materials was used. We could choose from quartz plates with anti-reflection coating and a thickness of 0.2 mm and 0.5 mm, uncoated microscope cover plates made of fused silica with a thickness of 0.1 mm and 0.3 mm, and fused silica plates with anti-reflection coating with a thickness of 1 mm, 2mm, and 3 mm. Starting from the 150 fs, 80  $\mu\text{J}$  output pulses after the cascaded second-order nonlinearity broadening and compression, we employed a convex lens with  $f=75$  mm to focus the beam. The plates

were placed at Brewster angle to minimize reflection losses. The distance between the focal point of the beam and the entrance surface of the plate was different for different plate thicknesses. To adjust the distance, the plate was placed behind the focus and moved towards the focus until spectral broadening was maximized, but before self-focusing happened inside the plate. In this way we could prevent beam collapse and material damage. Another critical point is supercontinuum generation, which starts close to self-focusing. When it sets in, the spectrum becomes unstable because the process of supercontinuum generation and the process of SPM compete. In some cases we combined two plates to achieve intermediate plate thicknesses. After adding a few plates the pulse energy reduced due to reflection losses and made refocusing necessary. Therefore we employed another convex lens with  $f=40$  mm.

After three broadening steps a FROG measurement revealed that the pulse acquires a considerable amount of chirp, which reduces spectral broadening. To compensate the chirp we employed a transmission grating pair (Thorlabs, GTI 25-03) with a groove density of  $300 \text{ mm}^{-1}$ . At the blaze angle of  $24.8^\circ$  and a grating distance of 10 mm the gratings introduce a GDD of  $-1700 \text{ fs}^2$  according to Eq. 3.4. The gratings transmit only 30 % of the energy and therefore complicate further spectral broadening in thin plates. With another convex lens with  $f=30$  mm we refocused the beam to see if further spectral broadening with an unchirped pulse is possible.

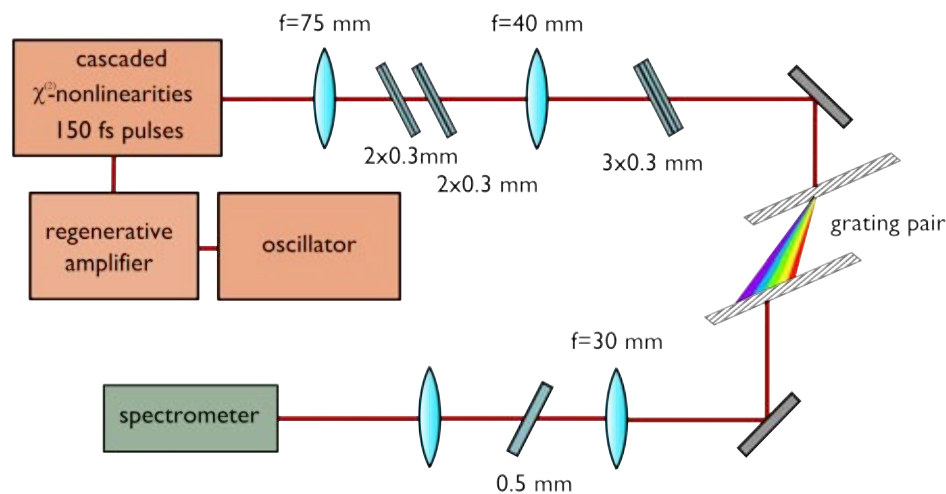


**Figure 5.1:** Sketch of the multiple thin plates broadening approach: The 150 fs input pulses are focused to a first set of 0.3 mm thick fused silica plates. After refocusing the pulses are sent to another combination of 0.3 mm thick plates. A grating compress compensates for the acquired chirp before the pulses are focused to a 0.5 mm thick plate.

Figure 5.1 shows a sketch of the setup for the broadest recorded spectrum. All spectra were recorded with an Ocean Optics HR 4000 spectrometer. The shape of the spectrum is very sensitive to the coupling of the beam into the spectrometer. Focusing the beam into the spectrometer decreased the sensitivity, but spectra recorded at different positions in the setup and on consecutive days are still difficult to compare.

## 5.3 Experimental results

To get an impression of the influence of the plate thickness on spectral broadening, we tested different combinations of plates. Starting from the thinnest available plate with a thickness of 0.1 mm we did not see any change in the spectrum. To increase the thickness, we combined first two and then three of the uncoated fused silica plates yielding a thickness of 0.2 mm and 0.3 mm, respectively. Only for the combination of three plates we noticed a change in the spectrum. By adding a fourth plate the spectrum broadened slightly more.

By focusing to the next thicker 0.2 mm quartz plate no apparent change in the spectrum occurred. Because of the quadratic shape of the quartz plates instead of the round shape of the fused silica plates we found no suitable mount to combine several plates. Therefore we used the next thicker quartz plate with a thickness of 0.5 mm. In this way we could achieve spectral broadening.

These results indicate that noticeable spectral broadening in our configuration starts from a plate thickness of about 0.3 mm. Lu et al. [24] in comparison achieved the best results with 0.1 mm thick fused silica plates, but used 6 times shorter pulses and a higher pulse energy.

### 5.3.1 Spectral broadening with 0.3 mm fused silica plates

Having 0.3 mm thick fused silica plates in place, we continued our studies with these plates. Figure 5.2-a shows the normalized spectra for different combinations of plates. For one plate we noticed spectral broadening (Fig. 5.2 -a, left, blue line), which could be increased by adding a second plate (green line). Adding a third plate revealed less change than adding the second plate. Because of their similarity the spectra are hard to analyze, so we integrated them. Figure 5.2-b shows the area under the normalized spectra for different plate thicknesses as well as the transmission. The area under the spectrum changes from 6.41 in a single plate to 6.70 in two plates and 6.75 in three plates. The transmission reduces from 93 % to 90 % and 84 %, respectively. Because the gain in spectral broadening for a third plate is negligible in comparison to the losses we decided to continue with the spectrum achieved in 0.6 mm fused silica.

Then we introduced a second combination of two 0.3 mm thick fused silica plates and moved it towards the first combination of plates. We could not reduce the distance between the plate combinations below 5 mm due to geometrical limitations. Figure 5.2-a shows the recorded spectrum (center, yellow line). The green line depicts the spectrum achieved with 0.6 mm thick plates as a comparison. The green spectrum is noticeably broader and more energy is coupled to the wings, which agrees with the theory of homogenization after refocusing. The area under the spectrum increases from 6.75 to 7.10. If the second plate combination consists of three instead of two plates the red spectrum was achieved. It is similar to the yellow spectrum but contains more energy in the center and less energy in the wings. The area under the red spectrum is 7.91. This number is misleading and can be explained by the raised center parts in comparison to the yellow spectrum. To keep the introduced material thickness small and to maximize the energy in the wings of the spectrum, we decided to continue with the combination of two 0.6 mm thick plates.

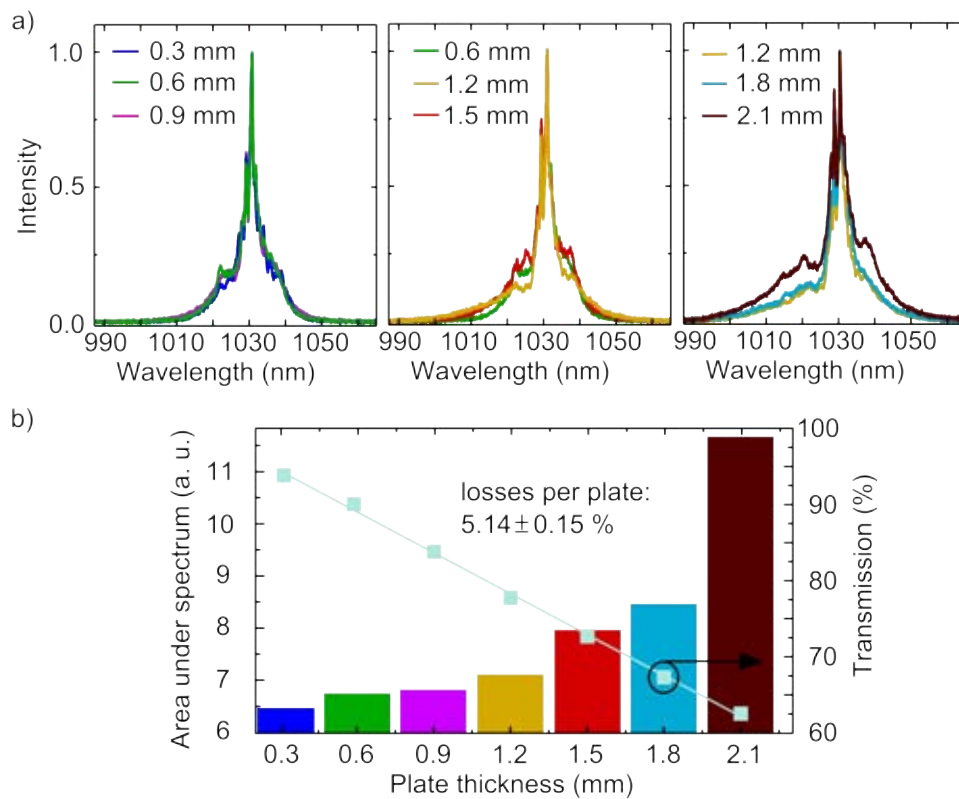


**Figure 5.2:** a) Normalized spectra recorded for different combinations of 0.3 mm thick fused silica plates. The combinations are explained in the main text. The mentioned thickness refers to the total thickness of material introduced. b) Calculated area under the measured spectra and according transmission. The blue line shows a linear fit of the transmission (blue squares). The slope indicates the averaged losses per plate.

In this configuration adding another combination of two plates could not increase the spectral width further. The reason is the reduced intensity due to reflection losses and beam divergence. Ideally a multiple thin plates setup should guide the beam and limit its beam width within the amplitude of small oscillations. In our case we could not optimize the plate distance due to geometrical limitations. Therefore we had to employ another lens to refocus. We placed a combination of two 0.3 mm thick plates after the focus of the lens and moved it towards the focus. Figure 5.2-a shows the broadest recorded spectrum (right, blue line). We could increase the area under the spectrum from 7.10 to 8.40. By using three instead of two 0.3 mm plates the area under the spectrum ran up to 11.61. The according brown spectrum contains much more energy in the wings of the spectrum.

In this configuration the transmission after the last plate is 63 %, which corresponds to a pulse energy of 50  $\mu\text{J}$ . The slope of the linear fit of the transmission (Fig. 5.2-b, blue line) is a measure for the average loss per plate. Every 0.3 mm of introduced fused silica the transmission drops by  $5.14 \pm 0.15\%$ .

### 5.3.2 Pulse compression

Neither increasing the thickness by adding another plate nor placing another plate combination behind the first one could increase the spectral width noticeably. Therefore we measured a FROG spectrogram of the pulse after the plates to analyze its spectral phase. Retrieving the spectrogram revealed that the pulse duration is still close to the input pulse duration of 150 fs. Due to the small amount of material introduced the pulse experiences almost no temporal broadening due to dispersion. From the spectral phase we could estimate a GDD of 2000  $\text{fs}^2$ . To compensate the chirp, we compressed the pulse using transmission gratings. With an introduced GDD of  $-1700 \text{fs}^2$  we achieved the best results. Figure 5.3 shows the measured (a) and reconstructed (c) spectrogram of the pulse after compression and its retrieved time envelope (b) and spectrum (d) as well as the temporal and spectral phase, respectively.

The compressed FWHM pulse duration is 58 fs which is only 4 fs longer than the FT limit pulse duration of 54 fs. The time envelope shows a weakly pronounced pedestal, but the main pulse contains 91 % of the total energy. This implies that the spectrum is well compressible and spatial filtering is not necessary.

### 5.3.3 Spatial characterization of the spectrum

Comparing the measured spectra depicted in Fig. 5.2-a and the retrieved spectrum depicted in Fig.5.3-d, we notice a difference in the spectral shape. The measured spectra show a pronounced peak around 1030 nm, whereas the retrieved spectrum shows two shoulders and a dip around 1030 nm.

To characterize the measured spectrum spatially we placed a closed pinhole in the center of the beam. The transmission dropped to 54 % and the peak in the spectrum disappeared. Figure 5.4-a shows the measured spectrum before the pinhole was introduced and afterwards. Both spectra were normalized. The spatially filtered spectrum is more homogeneous, has a broader FWHM and contains more energy in the wings. In Fig. 5.4-b the spatially filtered

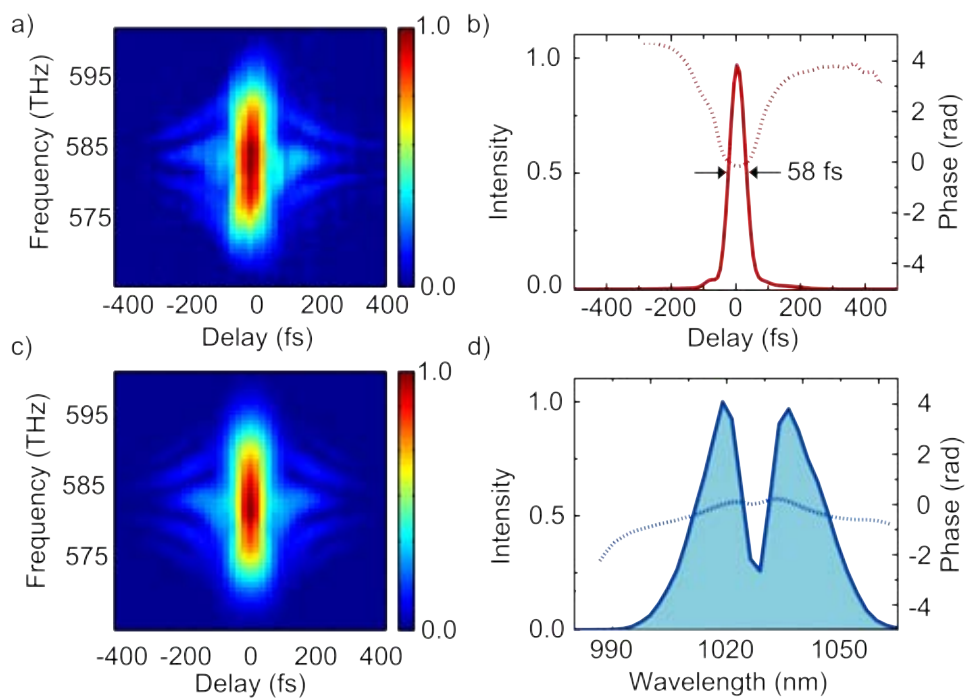


**Figure 5.3:** Pulse compression: Measured (a) and reconstructed spectrogram (c) of the pulse after compression.  $G_{error} = 1.0 \times 10^{-2}$ . b) Retrieved time envelope (solid red line) and phase (dashed red line). d) Retrieved spectrum (solid blue line) and spectral phase (dashed blue line).

spectrum was rescaled to match the shoulders of the unfiltered spectrum. The turquoise line shows the spectrum after the LBO crystal, which can be considered as the input spectrum. It is evident that the unfiltered spectrum can be decomposed into a part containing the peak at 1030 nm, which is represented by the input spectrum, and a part containing the shoulders, which is represented by the filtered spectrum. The decomposition shows that the outer part of the beam does not change while propagating through the thin plates, because its spectrum is similar to the input spectrum. The newly generated frequencies are contained in the center of the beam.

The pink line in Fig. 5.4-b shows the spectrum retrieved from the FROG measurement. It shows good agreement with the unfiltered spectrum when rescaling it to the same level. The agreement suggests that the FROG also acts as a spatial filter. Although the spectrogram was recorded without spatial filtering, only the intense center part of the beam generates a second harmonic, which is recorded as FROG signal.

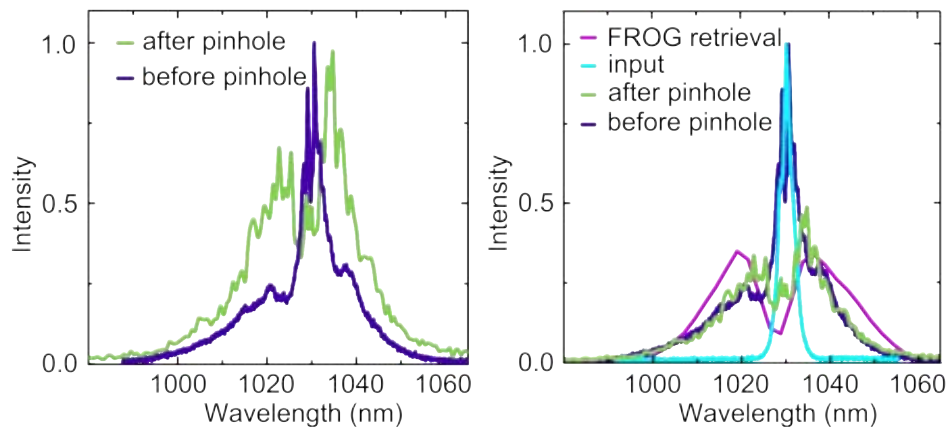


**Figure 5.4:** Spatial characterization of the broadened spectrum: a) Normalized spectra before a closed pinhole was placed in the center of the beam (purple) and afterwards (green). b) The spatially filtered spectrum (green) was rescaled to match the shoulders of the unfiltered spectrum (purple). The pink line shows the spectrum retrieved from the FROG measurement, which was also rescaled to the same level. The turquoise line shows the spectrum measured after the LBO crystal.

### 5.3.4 Further broadening after compression

To show that further spectral broadening is possible with the FT limited 58 fs pulses, we focused the beam to a 0.5 mm thick quartz plate. Figure 5.5 shows a comparison between the spectrum before the grating compressor and the spectrum after the added 0.5 mm plate.

Both spectra have the same shape: a strong peak around 1030 nm surrounded by two shoulders, whereof the red shoulder is higher than the blue shoulder. The shoulders are more weakly pronounced in the purple spectrum, which could also be an artifact of slightly different coupling into the spectrometer. The green spectrum extends from 980 nm to 1065 nm and

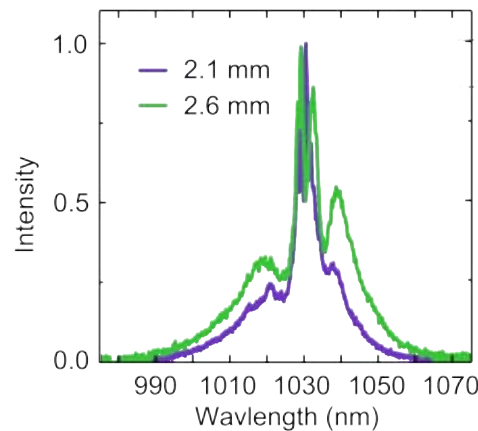


**Figure 5.5:** Comparison between the spectra before (purple) and after compression (green). The green spectrum was achieved by adding another 0.5 mm thick quartz plate. The calculated FT limit of this spectrum is 36 fs.

supports a FT limit pulse duration of 36 fs. The transmission of the 0.5 mm thick quartz plate was 80 %. Due to the high losses in the transmission gratings the pulse energy after the plate reduced to 11  $\mu\text{J}$ . Although with tight refocusing it was not possible to achieve further spectral broadening by placing additional plates behind the 0.5 mm plate. Due to the lack of more appropriate compression tools like chirped mirrors or high performance transmission gratings with suitable GDD, we could not increase the pulse energy. Therefore the green spectrum in Fig. 5.5 is up to now the broadest achieved spectrum.

## 5.4 Summary and conclusion

Spectral broadening in bulk is generally limited by the critical power for self-focusing. If self-focusing occurs, the beam collapses and conversion efficiency drops due to spatial losses. This can be circumvented by choosing the material length shorter than the critical self-focusing length. A setup consisting of an alternating sequence of thin glass plates and air gaps can provide beam guiding and holds promise to outperform fibers in terms of input energy and conversion efficiency. This is highly desirable because an all-solid state spectral broadening approach is more compact, more robust, and more cost-effective than any other spectral broadening technique.

Our first preliminary experiments conducted with 150 fs pulses suggest that the optimum plate thickness for a multiple plates approach for this pulse duration lies between 0.5 mm and 0.6 mm. To assure this number, more experimental as well as numerical studies have to be done. By employing three fused silica plates with a thickness of 0.6 mm, 0.6 mm, and 0.9 mm thickness we could broaden the spectrum to extend from 990 nm to 1060 nm. The spectrum is well compressible to 58 fs, which corresponds to a compression factor of nearly three. The transmission of the plate combination is 63 %. Although the spectrum is not spatially homogeneous, compression without filtering leads to a pulse with only 9 % of the total

energy contained in the pedestal.

After compression we could further broaden the spectrum by focusing the beam to a 0.5 mm thick quartz plate. The measured spectrum ranges from 980 nm to 1065 nm and supports a FT limit pulse duration of 36 fs. Due to the low transmission of the grating compressor the pulse energy is limited to 11  $\mu\text{J}$  which prevents further spectral broadening in thin plates.

Our experiments showed that the multiple thin plates method is applicable to 150 fs pulses. The results are promising but to assess the possible optimum performance of the approach more detailed measurements need to be conducted. Especially when it comes to the spatial homogeneity of the spectrum and in this context the spatial losses, measurements have to be redone considering that the input pulse is also not spatially homogeneous (see Chapter 4). To continue the research, one should first think of a more flexible way to mount plates of different shape and thickness, which allows the limitless adjustability of the plate distance.

# Chapter 6

## Conclusion and outlook

With the advent of third-generation femtosecond technology the demand for suitable compression techniques for 1ps pulses grew. Since common methods like spectral broadening in fibers or bulk show major drawbacks when operated with 1 ps pulses, this thesis presents two alternative approaches based on cross-polarized wave generation and cascaded second-order nonlinearities.

The first approach employs a cascaded setup consisting of two XPW stages which enables pulse shortening by a factor of 3. The output pulses are shorter than 250 fs and comprise pulse compression, temporal contrast enhancement, spectral smoothing and spatial beam profile cleaning. Although the pulses generated in XPW are intrinsically shortened by  $\sqrt{3}$ , we found that at high input intensities other nonlinear third-order processes like SPM and XPM are enabled. An interplay of both processes leads to additional spectral broadening and introduces a nonlinear spectral phase. The XPW process itself does not affect the spectral phase. In experiment as well as in simulation we showed that the introduced chirp reduces spectral broadening and pulse shortening in the second XPW stage. To compensate the chirp we operated a grating compressor between both XPW stages. In this configuration we achieved a compression rate of 4.

The main drawback of cascaded XPW is the low total conversion efficiency. As it is a third-order process, the conversion efficiency in XPW depends on the third-order susceptibility, which is in general many orders of magnitudes smaller than the second-order susceptibility. Therefore the reported conversion efficiency in a single crystal for Gaussian input pulses never exceeded 15 % [81]. For a cascaded setup this means a conversion efficiency of 2 %. The conversion efficiency also scales with the square of the input intensity and the square of the crystal length. Since the damage threshold of material depends inversely on the square of the pulse duration, the input intensity for 1 ps pulses is rather limited. Furthermore the crystal length cannot be extended limitless, because when it exceeds the critical self-focusing length material damage happens via self-focusing. One way out could be a two-crystal arrangement which avoids self-focusing. For this approach a maximum conversion efficiency of 20 % was reported [66], which could lead to doubling of the total conversion efficiency of cascaded XPW.

The second approach is based on cascaded second-order nonlinearities. In phase mismatched SHG the fundamental experiences a phase shift followed by self-focusing and spectral broadening. Temporal recompression requires dispersive elements. In the used setup spectral broadening of the fundamental in a phase mismatched SHG crystal is followed by a transmission grating compressor. Both steps are repeated to generate 150 fs output pulses, which correspond to a compression rate of above 6. As we observed that the output pulse duration decreases with increasing input intensity, even higher compression rates are possible. The total transmission of the setup is 45 % and can be improved up to 60 % by optimizing the crystal type, the crystal length and the dispersive elements.

Because phase mismatched SHG is an unsaturated process the generated second harmonic is temporally shortened by  $\sqrt{2}$ . This makes the reuse of the frequency doubled by-product attractive for filamentation in bulk or fiber.

Besides these promising results it must be mentioned that the spectrum of the broadened fundamental is not spatially homogeneous. The newly generated frequencies are contained in the center of the beam profile. The less intense outer part of the beam is not affected by spectral broadening. Thus the spectral shape is inhomogeneous and shows a pronounced peak centered at the input frequency. Nevertheless temporal compression worked well without spatial filtering in our case.

Comparing both methods at first sight cascaded second-order nonlinearities are more attractive, because of the impressive conversion efficiency and the higher compression rate. Another advantage is the possibility of reusing the frequency doubled by-product. Both methods are scalable in energy, but pulse shortening in cascaded XPW is in principal independent of the input intensity. In cascaded second-order nonlinearities the compression rate increases with increasing input intensity. Therefore varying the input energy requires readjustment of the beam size on the crystal. Another advantage of cascaded XPW is the spatial beam profile enhancement and spectral smoothening. Cascaded second order nonlinearities instead, deteriorate the spatial beam quality and the spectral shape. After all the XPW signal is intrinsically shorter whereas the spectrally broadened fundamental in cascaded second-order nonlinearities requires dispersive elements to be recompressed in time. This leads to a more complex setup and losses are increased.

This comparison revealed that the XPW process has very desirable properties, but the low conversion efficiency in a cascaded setup restricts its applicability. The presented setup for cascaded second-order nonlinearities generates energetic 150 fs pulses. These pulses are a good starting point for continuum generation.

To optimize the pulse compression technique for 1 ps pulses one could think of a combination of both methods. Starting from spectral broadening in phase mismatched SHG followed by a compression stage the shortened pulses will be sent to a XPW stage. A repetition of phase mismatched SHG and compression before XPW is also possible. The shorter input pulses for XPW will help to increase the conversion efficiency of the process. After the XPW process the output pulses will be spatially filtered, spectrally smoothened and additionally shortened by  $\sqrt{3}$ .

To further broaden the 150 fs pulses we tested a novel method for continuum generation based on a multiple thin plates setup. By limiting the plate thickness the input power can exceed the critical power for self-focusing by many multiples because beam collapse due to self-focusing inside the material is avoided. If the plate thickness and plate distance is chosen carefully this approach can provide beam guiding and holds promise to outperform fiber technology in terms of input power and conversion efficiency. Furthermore it is more compact, less alignment-sensitive, and more cost-effective.

In our experiment we could generate a spectrum ranging from 980 nm to 1065 nm by employing four thin plates. The spectrum supports a FT limit pulse duration of 36 fs but shows spatial inhomogeneity. It needs to be analyzed if the spatial inhomogeneity can be reduced if the input spectrum is more homogeneous. Of course more experimental as well as numerical studies have to be done to optimize the plate thickness, the plate distance and the beam divergence.

For further experimental optimization an appropriate mount for plates of different shape and thickness must be designed. The most important requirement for the design is the continuous adjustability of all plate distances without geometrical limitations. Therefore a ray with thin sliding mounts could be one possibility.

Multiple thin plates spectral broadening is a very promising method and its frontiers cannot be estimated yet. Lu et al. [82] managed to compress 25 fs input pulses to 2.8 fs in a setup consisting of four thin plates. Taking their results and our preliminary experiments into account the compression of 150 fs to 10 fs or less is feasible with multiple thin plates. Due to the acquired chirp temporal recompression might become necessary after four or five plates. With chirped mirrors the compression is possible at high conversion efficiency.

The output pulses of the proposed setup will be short enough to allow efficient broadband difference-frequency generation in short crystals. The DFG process guarantees the CEP-stability of the broadband spectrum and shifts it to the IR to range from 1500 nm to 2500 nm. After recompression the pulse is sent to a HCF to extend the spectrum to the visible. In this way we generate a multioctave, CEP-stable supercontinuum spanning from 400 nm to 2.5  $\mu\text{m}$  and meet all requirements for the seed generation of the proposed multi-terawatt waveform synthesizer. This device will enable us to generate high harmonics at unseen energies and pave the way towards hard x-ray attosecond pulses.

# Appendix A

## Frequency-resolved optical gating: Measuring ultrashort pulses

The most important tool to experimentally investigate nonlinear processes and the influence of different quantities like the spectral phase is a technique to fully characterize ultrashort pulses. Frequency-resolved optical gating (FROG) was the first technique to provide access to all information contained in the electric field of the laser pulse [83]. In the frame of this work a second-harmonic-generation (SHG) FROG was implemented in the lab. The following chapter explains the working principles of this method.

### A.1 The phase-dilemma

Until 1992 there was no technique available to determine the time-dependent intensity  $I(t)$  and the phase  $\phi(t)$  of the complex electric field of an ultrashort laser pulse. Either the spectral intensity of the pulse  $S(\omega)$  was measured in the frequency domain, leading to an unsolvable one-dimensional phase-retrieval problem, or the intensity autocorrelation was measured in the time domain as an attempt to reconstruct the time-dependent intensity  $I(t)$  [84]. Since there are no shorter signals available than the pulses themselves, the only way out is to split the pulse and sample it with a delayed copy of itself. Spatially overlapping of both pulses in a nonlinear crystal reveals the intensity autocorrelation. However this measurement cannot give full information about the pulse shape since it is always symmetric. To retrieve the pulse duration, an initial guess of the pulse shape has to be made [85]. The FROG method combines both time and frequency domain to the so-called "time-frequency domain" and records the signal of the intensity autocorrelation with a spectrometer, yielding a spectrogram of the pulse. This leads to a two-dimensional phase-retrieval problem, which can be solved using iterative algorithms.

### A.2 Beam geometry of a second-harmonic-generation FROG

The beam geometry of a SHG-FROG is basically the same as for second order autocorrelation except that the signal is recorded by a spectrometer instead of a detector. A scheme of

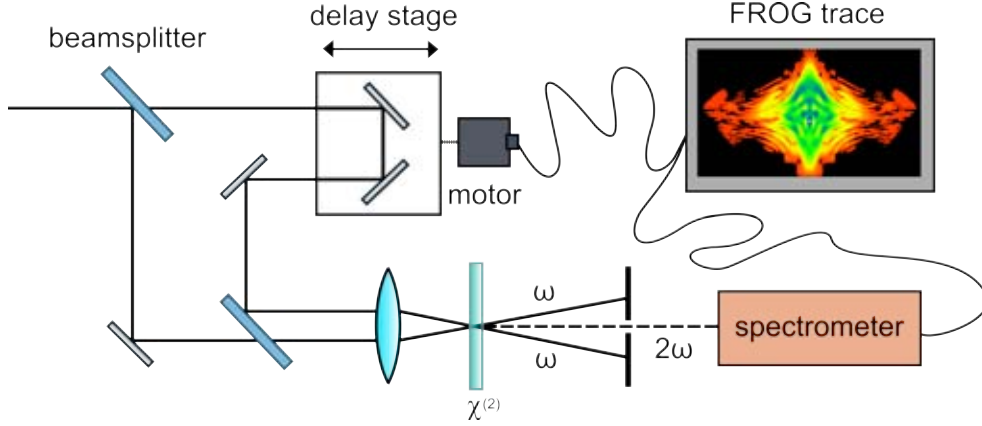


**Figure A.1:** Schematic beam geometry for a SHG-FROG: The incoming beam hits a beam splitter. One arm is delayed using a controllable delay stage. Both arms are spatially overlapped in a  $\chi^{(2)}$  crystal. The fundamental is filtered with a slit. The second harmonic is recorded with a spectrometer as a function of the delay.

a SHG-FROG is shown in Fig. A.1. The incoming beam hits a beam splitter. One path is delayed by a controllable delay stage. Both paths are focused into a SHG crystal ( $100 \mu\text{m}$  thick BBO) and spatially overlapped in the focus to produce an instantaneous response at twice the frequency of the input beam. The signal is filtered by a slit and sent to the spectrometer (Avantes AvaSpec 3648). In order to scan the delay stage, a Zaber T-Series motor is connected to a Labview-Program which reads out the spectrometer and generates the FROG trace. The latter shows the spectrogram of the pulse, i.e. the spectral intensity  $S(\omega)$  at each position of the delay stage according to a time-delay  $\tau$ . Since SHG is a second-order nonlinear process, the FROG traces are symmetric and therefore unintuitive to read. Consequentially there is an ambiguity in the direction of time. The way out is to use FROG geometries that rely on third-order nonlinear processes like polarization gating or transient gating. These geometries do not show any ambiguities and generate intuitive FROG traces, but have other drawbacks like being less sensitive and experimentally more complex [86].

### A.3 Retrieving the electric field from the spectrogram

As mentioned before, the FROG trace  $I_{FROG}^{SHG}(\omega, \tau)$  is the spectrally resolved signal of the second order intensity autocorrelation. That means it is the squared magnitude of the Fourier Transform of the intensity autocorrelation field  $E^{AC}(t, \tau)$  with respect to time.

$$I_{FROG}^{SHG}(\omega, \tau) = \left| \int_{-\infty}^{\infty} E^{AC}(t, \tau) \exp(-i\omega t) dt \right|^2 \quad (\text{A.1})$$

The intensity autocorrelation field  $E^{AC}(t, \tau)$  in the case of a second-order nonlinear process is simply

$$E^{AC}(t, \tau) \propto E(t)E(t - \tau). \quad (\text{A.2})$$

Therefore the spectrogram reads

$$I_{FROG}^{SHG}(\omega, \tau) = \left| \int_{-\infty}^{\infty} E(t)E(t-\tau)\exp(-i\omega t)dt \right|^2. \quad (\text{A.3})$$

Because in the case of SHG-FROG the pulse is gated with a delayed version of itself, the electric field  $E(t)$  cannot be retrieved using a spectrogram inversion algorithm. Rewriting expression A.3 however transforms the problem into a two-dimensional phase-retrieval problem. Instead of writing the intensity autocorrelation field  $E^{AC}(t, \tau)$  as the Fourier Transform of the new quantity  $\hat{E}^{AC}(t, \Omega)$  with respect to  $t$  we write it as the Fourier transform with respect to  $\tau$ .

$$E^{AC}(t, \tau) = \int_{-\infty}^{\infty} \hat{E}^{AC}(t, \Omega)\exp(-i\Omega\tau)d\Omega \quad (\text{A.4})$$

To retrieve  $E(t)$ , it is sufficient to find  $\hat{E}^{AC}(t, \Omega)$  because  $E^{AC}(t, \tau)$  is the inverse Fourier Transform of  $\hat{E}^{AC}(t, \Omega)$ . The substitution  $t = \tau$  yields

$$E^{AC}(t, t) = E(t)E(0), \quad (\text{A.5})$$

where  $E(0)$  is a negligible constant. Inserting equation A.4 into A.1 leads to

$$I_{FROG}^{SHG}(\omega, \tau) = \left| \int_{-\infty}^{\infty} \int_{-\infty}^{\infty} \hat{E}^{AC}(t, \Omega)\exp(-i\omega t)\exp(-i\Omega\tau)dt d\Omega \right|^2. \quad (\text{A.6})$$

Expression A.6 can be treated as a two-dimensional phase-retrieval problem which can be solved by iterative algorithms. The algorithm of generalized projections has proven to be the most reliable one [87]. Equation A.3 and equation A.2 are the two constraints that have to be fulfilled. The algorithm starts from an arbitrary signal field  $E(t)_{init}$  that most likely does not fulfill any of both constraints and projects it to the first constraint set. From this point it is projected to the second constraint set and back to the first set etc. Iterative projections between the two sets lead to the cross section of both sets which is the correct  $E(t)$ .

# Appendix B

## Simulation of the XPW process

The simulation of the XPW process is based on a Matlab-code from Hannieh Fattahi and Nick Karpowicz which solves the coupled wave equation 3.2 in a split-step method [88]. The code accounts for dispersion, diffraction and the third-order nonlinearity. It applies slowly evolving envelope approximation to propagate the input pulse along the crystal in cylindrical coordinates. The default input pulse is a Gaussian pulse in space and time with a pulse duration of 1 ps centered at 1030 nm. The center waist of the Gaussian beam  $w_0$  is 150  $\mu\text{m}$  ( $D_{FWHM}$ ). The simulation starts 100 mm after the focal point immediately in the crystal. The peak intensity at the starting point of the simulation ranges from 180  $\text{GW}/\text{cm}^2$  to 450  $\text{GW}/\text{cm}^2$  and reaches similar output conversion efficiency than in experiment. It is assumed that  $\chi^{(3)} = 1.59 \cdot 10^{22} \text{m}^2/\text{V}^2$  for  $\text{BaF}_2$  [66]. Unless specified otherwise the crystal length is 6 mm.

The code was modified to calculate an input pulse based on the retrieved spectrum from FROG measurements. This opens the possibility to run the program in two different modes. In the first mode the the time-envelope of the input pulse is calculated by Fourier transforming the measured spectrum with spectral phase zero. In this case the input pulse is FT limited. In the second mode the time-envelope is calculated by Fourier transforming the spectrum with the spectral phase retrieved from the FROG measurement to end up with a chirped input pulse. The accuracy of this feature was proven by comparing the simulation results for the first mode and a Gaussian input pulse with the same pulse duration.

Besides this modification the possibility to simulate the cascaded XPW process was implemented. In this case the generated output XPW pulse after the first crystal is taken as the input pulse for the second crystal. The beam waist on the second crystal is calculated to achieve the same peak intensity on both crystals.

# Bibliography

- [1] T. H. Maiman, “Stimulated optical radiation in ruby,” *Nature*, vol. 187, no. 4736, pp. 493–494, 1960.
- [2] P.-T. Ho, L. A. Glasser, E. P. Ippen, and H. A. Haus, “Picosecond pulse generation with a cw GaAlAs laser diode,” *Applied Physics Letters*, vol. 33, no. 3, pp. 241–242, 1978.
- [3] T. Barbec, C. Spielmann, P. F. Curley, and F. Krausz, “Kerr lens mode locking,” *Optics Letters*, vol. 17, no. 18, pp. 1292–1294, 1992.
- [4] A. Baltuska, M. S. Pshenichnikov, R. Szipoecs, and D. A. Wiersma, “A compact all-solid-state sub-5-fsec laser,” *Optics and Photonics News*, vol. 8, no. 12, pp. 46–47, 1997.
- [5] M. Drescher, M. Hentschel, R. Kienberger, G. Tempea, C. Spielmann, G. A. Reider, P. B. Corkum, and F. Krausz, “X-ray pulses approaching the attosecond frontier,” *Science*, vol. 291, pp. 1923–1927, 2001.
- [6] P. Corkum, “Braking the attosecond barrier,” *Optics and Photonics News*, vol. 6, no. 5, pp. 18–22, 1995.
- [7] P. M. Paul, E. S. Toma, P. Breger, G. Mullot, F. Auge, P. Balcou, H. G. Muller, and P. Agostini, “Observation of a train of attosecond pulses from high harmonic generation,” *Science*, vol. 292, pp. 1689–1692, 2001.
- [8] M. Hentschel, R. Kienberger, C. Spielmann, G. A. Reider, N. Milosevic, T. Brabec, P. Corkum, U. Heinzman, M. Drescher, and F. Krausz, “Attosecond metrology,” *Nature*, vol. 414, pp. 509–513, 2001.
- [9] F. Krausz and M. Ivanov, “Attosecond physics,” *Review of Modern Physics*, vol. 81, pp. 166–234, 2009.
- [10] M. Drescher, M. Hentschel, R. Kienberger, M. Uiberacker, V. Yakovlev, A. Scrinzi, T. Westerwalbesloh, U. Kleineberg, U. Heinzmann, and F. Krausz, “Time-resolved atomic inner-shell spectroscopy,” *Nature*, vol. 419, pp. 803–807, 2002.
- [11] J. Itatani, J. Levesque, D. Zeidler, H. Niikura, H. Pepin, J. C. Kieffer, P. B. Corkum, and D. M. Villeneuve, “Tomographic imaging of molecular orbitals,” *Nature*, vol. 432, pp. 867–871, 2004.

- [12] T. Kanai, S. Minemoto, and H. Sakai, "Quantum interference during high-order harmonic generation from aligned molecules," *Nature*, vol. 435, pp. 470–474, 2005.
- [13] S. Kumar, H.-S. Kang, and D. E. Kim, "Generation of isolated single attosecond hard X-ray pulse in enhanced self-amplified spontaneous emission scheme," *Optics Express*, vol. 19, no. 8, pp. 7537–7545, 2011.
- [14] A. L. Cavalieri, E. Goulielmakis, B. Horvath, W. Helml, M. Schultze, M. Fiess, V. Pervak, L. Veisz, V. S. Yakovlev, M. Uiberacker, A. Apolonski, F. Krausz, and R. Kienberger, "Intense 1.5-cycle near infrared laser waveforms and their use for the generation of ultra-broadband soft-x-ray harmonic continua," *New Journal of Physics*, vol. 9, 2007.
- [15] A. Moulet, V. Tosa, and E. Goulielmakis, "Coherent kiloelectronvolt x-rays generated by subcycle optical drivers: a feasibility study," *Optics Letters*, vol. 39, no. 21, pp. 6189–6192, 2014.
- [16] H.-S. Chan, Z.-M. Hsieh, W.-H. Liang, A. H. Kung, C.-K. Lee, C.-J. Lai, R.-P. Pan, and L.-H. Peng, "Synthesis and measurement of ultrafast waveforms from five discrete optical harmonics," *Science*, vol. 331, pp. 1165–1168, 2011.
- [17] M. T. Hassan, A. Wirth, I. Grguras, A. Moulet, T. T. Luu, J. Gagnon, V. Pervak, and E. Goulielmakis, "Attosecond photonics: Synthesis and control of light transients," *Review of Scientific Instruments*, vol. 83, no. 111301, 2012.
- [18] H. Fattahi, A. Alismail, H. Wang, J. Brons, O. Pronin, T. Buberl, L. Vámos, G. Arisholm, A. M. Azzeer, and F. Krausz, "High-power, 1-ps, all Yb:YAG thin-disk regenerative amplifier," *Optics Letters*, vol. 41, no. 6, pp. 1126–1129, 2016.
- [19] T. Popmintchev, M.-C. Chen, D. Popmintchev, P. Arpin, S. Brown, S. Alisauskas, G. Andriukaitis, T. Balciunas, O. D. Mücke, A. Pugzlys, A. Baltuska, B. Shim, S. E. Schrauth, A. Gaeta, C. Hernandez-Garcia, L. Plaja, A. Becker, A. Jaron-Becker, M. M. Murnane, and H. C. Kapteyn, "Bright coherent ultrahigh harmonics in the keV X-ray regime from mid-infrared femtosecond lasers," *Science*, vol. 336, pp. 1287–1291, 2012.
- [20] C. Y. Teisset, M. Schultze, R. Bessing, M. Häfner, S. Prinz, D. Sutter, and T. Metzger, "300 W picosecond thin-disk regenerative amplifier at 10 kHz repetition rate," *Advanced Solid-State Lasers Congress Postdeadline Paper*, vol. JTh5A.1, 2013.
- [21] H. Fattahi, *Third-generation femtosecond technology*. PhD thesis, Ludwig-Maximilians-Universität Munich, 2014.
- [22] H. Fattahi, H. G. Barros, M. Gorjan, T. Nubbemeyer, B. Alsaif, C. Y. Teisset, M. Schultze, S. Prinz, M. Häfner, M. Ueffing, A. Alismail, L. Vámos, A. Schwarz, O. Pronin, J. Brons, X. T. Geng, G. Arisholm, M. Ciappina, V. S. Yakovlev, D.-E. Kim, A. M. Azzeer, N. Karpowicz, D. Sutter, Z. Major, T. Metzger, and F. Krausz, "Third-generation femtosecond technology," *Optica*, vol. 1, no. 1, pp. 45 – 63, 2014.

- [23] J. Moses, H. Suchowski, and F. X. Kärtner, "Fully efficient adiabatic frequency conversion of broadband Ti:sapphire oscillator pulses," *Optics Letters*, vol. 37, no. 9, pp. 1589–1591, 2012.
- [24] C.-H. Lu, Y.-J. Tsou, H.-Y. Chen, B.-H. Chen, Y.-C. Cheng, S.-D. Yang, M.-C. Chen, C.-C. Hsu, and A. H. Kung, "Generation of intense supercontinuum in condensed media," *Optica*, vol. 1, no. 6, pp. 400–406, 2014.
- [25] J. C. Knight, T. A. Birks, P. S. J. Russell, and D. M. Atkin, "All-silica single-mode optical fiber with photonic crystal cladding," *Optics Letters*, vol. 21, no. 19, pp. 1547–1549, 1996.
- [26] D. Mogilevtsev, T. A. Birks, and P. S. J. Russell, "Group-velocity dispersion in photonic crystal fibers," *Optics Letters*, vol. 23, no. 21, 1998.
- [27] T. A. Birks, J. C. Knight, and P. S. J. Russell, "Endlessly single-mode photonic crystal fiber," *Optics Letters*, vol. 22, no. 13, 1997.
- [28] T. Suedmeyer, F. Brunner, E. Innerhofer, R. Paschotta, K. Furusawa, J. C. Baggett, T. M. Monro, D. J. Richardson, and U. Keller, "Nonlinear femtosecond pulse compression at high average power levels by use of a large-mode-area holey fiber," *Optics Letters*, vol. 28, no. 20, 2003.
- [29] J. M. Dudley and G. G. and St Coen, "Supercontinuum generation in photonic crystal fiber," *Reviews of Modern Physics*, vol. 78, 2006.
- [30] J. K. Ranka, R. S. Windeler, and A. J. Stentz, "Visible continuum generation in air silica microstructure optical fibers with anomalous dispersion at 800 nm," *Optics Letters*, 2000.
- [31] J. M. Dudley and S. Coen, "Coherence properties of supercontinuum spectra generated in photonic crystal and tapered optical fibers," *Optics Letters*, vol. 27, no. 13, pp. 1180–1182, 2002.
- [32] J. W. Nicholson and M. F. Yan, "Cross-coherence measurements of supercontinua generated in highly-nonlinear, dispersion shifted fiber at 1550 nm," *Optics Express*, vol. 12, no. 4, 2004.
- [33] J. C. Travers, W. Chang, J. Nold, N. Y. Joly, and P. S. J. Russell, "Ultrafast nonlinear optics in gas-filled hollow-core photonic crystal fibers," *Journal of the Optical Society of America B*, vol. 28, no. 12, 2011.
- [34] M. Nisoli, S. De Silvestri, O. Svelto, "Generation of high energy 10 fs pulses by a new pulse compression technique," *Applied Physics Letters*, vol. 20, no. 68, 1996.
- [35] M. Nisoli, S. Stagira, S. D. Silvestri, O. Svelto, S. Sartania, Z. Cheng, M. Lenzner, C. Spielmann, and F. Krausz, "A novel-high energy pulse compression system: generation of multigigawatt sub-5-fs pulses," *Applied Physics B: Lasers and Optics*, vol. 65, no. 2, pp. 189–196, 1997.

- [36] S. Bohman, A. Suda, T. Kanai, S. Yamaguchi, and K. Midorikawa, "Generation of 5.0 fs, 5.0 mJ pulses at 1 kHz using hollow-fiber pulse compression," *Optics Letters*, vol. 35, no. 11, pp. 1887–1889, 2010.
- [37] J. S. Robinson, C. A. Haworth, H. Teng, R. A. Smith, J. P. Marangos, and J. W. G. Tisch, "The generation of intense, transform-limited laser pulses with tunable duration from 6 to 30 fs in a differentially pumped hollow fibre," *Applied Physics B: Lasers and Optics*, vol. 85, pp. 525–529, 2006.
- [38] F. Couny, F. Benabid, P. J. Roberts, P. S. Light, and M. G. Raymer, "Generation and photonic guidance of multioctave optical-frequency combs," *Science*, vol. 318, 2007.
- [39] K. F. Mak, J. C. Travers, N. Y. Joly, A. Abdolvand, and P. S. J. Russell, "Two techniques for temporal pulse compression in gas-filled hollow-core kagome photonic crystal fiber," *Optics Letters*, vol. 38, no. 18, 2013.
- [40] K. F. Mak, M. Seidel, O. Pronin, M. H. Frosz, A. Abdolvand, V. Pervak, A. Apolonski, F. Krausz, J. C. Travers, and P. S. J. Russell, "Compressing  $\mu\text{J}$ -level pulses from 250 fs to sub-10 fs at 38-MHz repetition rate using two gas-filled hollow-core photonic crystal fiber stages," *Optics Letters*, vol. 40, no. 7, 2015.
- [41] O. H. Heckl, C. J. Saraceno, C. R. E. Baer, T. Suedmeyer, Y. Y. Wang, Y. Cheng, F. Benabid, and U. Keller, "Temporal pulse compression in a xenon-filled Kagome-type hollow-core photonic crystal fiber at high average power," *Optics Express*, vol. 19, no. 20, 2011.
- [42] V. Petrov, W. Rudolph, and B. Wilhelmi, "Compression of high-energy femtosecond light pulses by self-phase modulation in bulk media," *Journal of Modern Optics*, vol. 36, no. 5, pp. 587–595, 1989.
- [43] A. L. Gaeta, "Catastrophic collapse of ultrashort pulses," *Physical Review Letters*, vol. 84, no. 16, pp. 3582–3585, 2000.
- [44] M. Seidel, J. Brons, V. Pervak, A. Apolonski, O. Pronin, and F. Krausz, "Double-stage spectral broadening in bulk crystals of 50 W, 1.3  $\mu\text{J}$ , 250 fs pulses to a Fourier transform limit of 15 fs," in *Nonlinear Optics*, (Kauai, Hawaii, United States of America), 2015.
- [45] L. Sudrie, A. Couairon, M. Franco, B. Lamouroux, B. Prade, S. Tzortzakis, and A. Mysyrowicz, "Femtosecond laser-induced damage and filamentary propagation in fused silica," *Physical Review Letters*, vol. 89, 2002.
- [46] A. H. Kung, C.-H. Lu, and Y.-C. Cheng, "Intense supercontinuum generation in condensed media," in *Nonlinear Optics*, (Kuaia, Hawaii, United States of America), 2015.
- [47] C. Rolland and P. B. Corkum, "Compression of high-power optical pulses," *Journal of the Optical Society of America B*, vol. 5, no. 3, pp. 641–647, 1988.
- [48] M. K. Reed, M. K. Steiner-Shepard, and D. K. Negus, "Widely tunable femtosecond optical parametric amplifier at 250 kHz with a Ti:sapphire regenerative amplifier," *Optics Letters*, vol. 19, no. 22, pp. 1855–1857, 1994.

- [49] M. Bradler, P. Baum, and E. Riedle, "Femtosecond continuum generation in bulk laser host materials with sub- $\mu\text{J}$  pump pulses," *Applied Physics B: Lasers and Optics*, vol. 91, pp. 561–574, 2009.
- [50] F. Silva, D. R. Austin, A. Thai, M. Baudisch, M. Hemmer, D. Faccio, A. Couairon, and J. Biegert, "Multi-octave supercontinuum generation from mid-infrared filamentation in a bulk crystal," *Nature Communications*, vol. 3, no. 807, pp. 1–5, 2012.
- [51] A. Couairon, J. Biegert, C. P. Hauri, W. Kornelis, F. W. Helbing, U. Keller, and A. Mysyrowicz, "Self-compression of ultra-short laser pulses down to one optical cycle by filamentation," *Journal of Modern Optics*, vol. 53, no. 1, pp. 75–85, 2006.
- [52] M. Bradler and E. Riedle, "Supercontinuum generation in laser host materials with pulse durations over the entire femtosecond regime," in *CLEO Europe*, (Munich, Germany), 2011.
- [53] A. I. Kovrighin, D. V. Yakovlev, B. V. Zhdanov, and N. I. Zheludev, "Self-induced optical activity in crystals," *Optics Communications*, vol. 35, no. 1, pp. 92–95, 1980.
- [54] A. Jullien, S. Kourtev, O. Albert, G. Chériaux, J. Etchepare, N. Minkovski, and S. M. Saltiel, "Highly efficient temporal cleaner for femtosecond pulses based on cross-polarized wave generation in a dual crystal scheme," *Applied Physics B: Lasers and Optics*, vol. 84, 2006.
- [55] A. Cotel, A. Jullien, N. Forget, O. Albert, C. L. Blanc, J. Etchepare, G. Chériaux, N. Minkovski, and S. M. Saltiel, "Nonlinear temporal pulse cleaning for high-energy petawatt-class lasers," *Journal de Physique IV*, vol. 133, pp. 713–715, 2006.
- [56] A. Jullien, L. Canova, O. Albert, D. Boschetto, L. Antonucci, Y.-H. Cha, J. P. Rousseau, P. Chaudet, G. C. Eriaux, J. Etchepare, S. Kourtev, N. Minkovski, and S. M. Saltiel, "Spectral broadening and pulse duration reduction during crosspolarized wave generation: influence of the quadratic spectral phase," *Applied Physics B: Lasers and Optics*, vol. 87, no. 4, pp. 595–601, 2007.
- [57] N. Minkovski, S. M. Saltiel, G. I. Petrov, O. Albert, and J. Etchepare, "Polarization rotation induced by cascaded third-order processes," *Optics Letters*, vol. 27, no. 22, pp. 2025–227, 2002.
- [58] N. Minkovski, G. I. Petrov, S. M. Saltiel, O. Albert, and J. Etchepare, "Nonlinear polarization rotation and orthogonal polarization generation experienced in a single-beam configuration," *Journal of the Optical Society of America B*, vol. 21, no. 9, pp. 1659–1664, 2004.
- [59] K. Osvay, L. Canova, A. P. Kovács, A. Börzsönyi, O. Albert, and R. L. Martens, "Preservation of the carrier envelope phase in generation of cross polarized wave," *Optics Express*, vol. 17, no. 25, pp. 22358–22365, 2009.

- [60] A. Cotel, A. Jullien, N. Forget, O. Albert, G. Chériaux, and C. L. Blanc, “Nonlinear temporal pulse cleaning of a 1-micrometer optical parametric chirped-pulse amplification system,” *Applied Physics B: Lasers and Optics*, vol. 83, pp. 7–10, 2006.
- [61] A. Jullien, O. Albert, F. Burgy, G. Hamoniaux, J.-P. Rousseau, J.-P. Chambaret, F. Augé-Rochereau, G. Chériaux, J. Etchepare, N. Minkovski, and S. M. Saitiel, “ $10^{-10}$  temporal contrast for femtosecond ultraintense lasers by cross-polarized wave generation,” *Optics Letters*, vol. 30, no. 8, pp. 920–922, 2005.
- [62] L. Canova, *Generation and shaping of ultra-short, ultra-high contrast pulses for high repetition rate relativistic optics*. PhD thesis, École Polytechnique Paris, 2009.
- [63] L. Canova, O. Albert, N. Forget, B. Mercier, S. Kourtev, N. Minkovski, S. M. Saitiel, and R. L. Martens, “Influence of spectral phase on cross-polarized wave generation with short femtosecond pulses,” *Applied Physics B: Lasers and Optics*, vol. 93, no. 2, pp. 443–453, 2008.
- [64] A. Jullien, O. Albert, G. Chériaux, J. Etchepare, S. Kourtev, N. Minkovski, and S. M. Saitiel, “Nonlinear polarization rotation of elliptical light in cubic crystals, with application to cross-polarized wave generation,” *J. Opt. Soc. Am.*, vol. 22, no. 12, pp. 2635–2641, 2005.
- [65] L. Canova, S. Kourtev, N. Minkovski, A. Jullien, R. Lopez-Martens, O. Albert, and S. M. Saitiel, “Efficient generation of cross-polarized femtosecond pulses in cubic crystals with holographic cut orientation,” *Appl. Phys. Lett.*, vol. 92, 2008.
- [66] A. Jullien, O. Albert, G. Chériaux, J. Etchepare, S. Kourtev, N. Minkovski, and S. M. Saitiel, “Two crystal arrangement to fight efficiency saturation in cross-polarized wave generation,” *Optics Express*, vol. 14, no. 7, pp. 2760–2769, 2006.
- [67] M. Lenzner, J. Krüger, S. Sartania, Z. Cheng, C. Spielmann, G. Mourou, W. Kautek, and F. Krausz, “Femtosecond optical breakdown in dielectrics,” *Physical Review Letters*, vol. 80, no. 18, pp. 4076–4079, 1998.
- [68] J. Su and G. Feng, “Analytical expressions for group-delay dispersion and third-order dispersion of a reflection grism-pair compressor,” *Applied Optics*, vol. 51, no. 14, pp. 2747–2751, 2012.
- [69] R. D. Salvo, D. J. Hagan, M. Sheik-Bahae, G. Stegman, and E. W. V. Styrland, “Self-focusing and self-defocusing by cascaded second-order effects in KTP,” *Optics Letters*, vol. 17, no. 1, 1992.
- [70] X. Liu, L. Qian, and F. Wise, “High-energy pulse compression by use of negative phase shifts produced by the cascade  $\chi^{(2)}:\chi^{(2)}$  nonlinearity,” *Optics Letters*, vol. 24, no. 23, 1999.
- [71] T. F. Carruthers and I. N. Duling, “Passive laser mode locking with an antiresonant nonlinear mirror,” *Optics Letters*, vol. 15, no. 14, pp. 804–806, 1990.

- [72] G. Cerullo, S. D. Silvestri, A. Monguzzi, D. Segala, and V. Magni, "Self-starting mode locking of a cw Nd:YAG laser using cascaded second-order nonlinearities," *Optics Letters*, vol. 20, no. 7, pp. 746–748, 1995.
- [73] H. J. Bakker, P. C. M. Planken, L. Kuipers, and A. Lagendijk, "Phase modulation in second-order nonlinear-optical processes," *Physical Review A: Atomic, Molecular, and Optical Physics*, vol. 42, no. 7, pp. 4085–48101, 1990.
- [74] B. B. Zhou, A. Chong, F. W. Wise, and M. Bache, "Ultrafast and octave-spanning optical nonlinearities from strongly phase-mismatched quadratic interactions," *Physical Review Letters*, vol. 109, 2012.
- [75] G.-R. Lin, Y.-T. Lin, and C.-K. Lee, "Simultaneous pulse amplification and compression in all-fiber-integrated pre-chirped large-mode-area Er-doped fiber amplifier," *Optics Express*, vol. 15, no. 6, pp. 2993–2999, 2007.
- [76] M. Centurion, M. A. Porter, P. G. Kevrekidis, and D. Psaltis, "Nonlinearity management in optics: Experiment, theory, and simulation," *Physical Review Letters*, vol. 97, no. 3, 2006.
- [77] N. Milosevic, G. Tempea, and T. Brabec, "Optical pulse compression: bulk media versus hollow waveguides," *Optics Letters*, vol. 25, no. 9, pp. 672–674, 2000.
- [78] M. Seidel, G. Arisholm, J. Brons, V. Pervak, O. Pronin, and F. Krausz, "All solid-state spectral broadening: An average and peak power scalable method for compression of ultrashort pulses."
- [79] A.-L. Calendron, H. Cankaya, G. Cirmi, and F. X. Kärtner, "White-light generation with sub-ps pulses," *Optics Ex*, vol. 23, no. 11, pp. 13866–13879, 2015.
- [80] A. Sommer, *Ultrafast Strong Field Dynamics in Dielectrics*. PhD thesis, Ludwig-Maximilians-Universitaet Munich, 2015.
- [81] A. Jullien, J.-P. Rousseau, B. Mercier, L. Antonucci, O. Albert, G. Cheriaux, S. Kourtev, N. Minkovski, and S. M. Saltiel, "Highly efficient nonlinear filter for femtosecond pulse contrast enhancement and pulse shortening," *Optics Letters*, vol. 33, no. 20, 2008.
- [82] C.-H. Lu, B.-H. Chen, Y.-C. Cheng, and A. H. Kung, "Multi-plate generation and compression of an intense supercontinuum pulse," in *High-Intensity Lasers and High-Field Phenomena*, 2016.
- [83] R. Trebino and D. J. Kane, "Using phase retrieval to measure the intensity and phase of ultrashort pulses: frequency-resolved optical gating," *Journal of the Optical Society of America A, Optics and Image Science*, vol. 10, 1993.
- [84] R. Trebino, *Frequency-Resolved Optical Gating: The Measurement of Ultra Short Laser Pulses*. Kluwer Academic Publishers, 2000.
- [85] J. E. Rothenberg and D. Grischkowsky, "Measurement of optical phase with subpicosecond resolution by time-domain interferometry," *Optics Letters*, vol. 12, 1987.

- [86] R. Trebino, K. W. DeLong, D. N. Fittinghoff, J. N. Sweetser, M. A. Krumbuegel, B. A. Richman, and D. J. Kane, "Measuring ultrashort laser pulses in the time-frequency domain using frequency-resolved optical gating," *Rev. Sci. Instrum.*, vol. 68, no. 9, pp. 3277–3295, 1997.
- [87] K. W. D. Long, D. N. Fittinghoff, and R. Trebino, "Pulse retrieval in frequency-resolved optical gating based on the method of generalized projections," *Optics Letters*, vol. 19, 1994.
- [88] T. R. Taha and M. I. Ablowitz, "Analytical and numerical aspects of certain nonlinear evolution equations. II. Numerical, nonlinear Schrödinger equation," *Journal of Computational Physics*, vol. 55, no. 2, pp. 203–230, 1984.